




# Manipulating Nucleation Potency of Substrates by Interfacial Segregation: An Overview

Yun Wang <sup>1,\*</sup>, Shihao Wang <sup>1</sup>, Zhongping Que <sup>1</sup>, Changming Fang <sup>1</sup>, Teruo Hashimoto <sup>2</sup>, Xiaorong Zhou <sup>2</sup>, Quentin M. Ramasse <sup>3</sup> and Zhongyun Fan <sup>1</sup>

<sup>1</sup> Brunel Centre for Advanced Solidification Technology (BCAST), Brunel University London, Uxbridge UB8 3PH, UK

<sup>2</sup> School of Materials, University of Manchester, Manchester M13 9PL, UK

<sup>3</sup> Super STEM Laboratory, SciTech Daresbury Campus, Daresbury WA4 4AD, UK

\* Correspondence: yun.wang@brunel.ac.uk; Tel.: +44-01895-268536

**Abstract:** During solidification of metallic materials, heterogeneous nucleation occurs on substrates, either endogenous or exogenous. The potency of the substrates for nucleation is mainly dependent upon the atomic arrangements on the substrate surface, which are affected by the lattice misfit between the substrate and the nucleated solid, the surface roughness at atomic scale, and the chemical interaction between the substrates and the melt. Extensive examinations on metal/substrate (M/S) interfaces at atomic scale by the state-of-the-art aberration (Cs) corrected STEM and associated EDS and EELS have shown that alloying elements in liquid melts tend to segregate at the interfaces, leading to the formation of various 2-dimensional compounds (2DCs) or 2-dimensional solutions (2DSs), depending upon segregation behavior of the elements. For instance, Al<sub>3</sub>Ti 2DC and Ti<sub>2</sub>Zr 2DC at the Al/TiB<sub>2</sub> interface, Y<sub>2</sub>O<sub>3</sub> 2DC at the Mg/MgO interface, and a Si-rich 2DS layer at Al-Si/TiB<sub>2</sub> interface have been identified. Such interfacial segregations significantly affect nucleation potency of the substrates, resulting in either promoting or impeding the heterogeneous nucleation process during solidification. In this paper, we present an overview of the current studies of interfacial segregation behavior, the structure and chemistry of interfaces, and their impacts on the subsequent heterogeneous nucleation and grain initiation processes. Our focus is on the advances made in the understanding of the mechanisms for nucleation and grain refinement. It is demonstrated that it is feasible to manipulate heterogeneous nucleation by modifying nucleation potency of a substrate through deliberate interfacial segregation of desirable elements, achieving effective control of the grain structure of cast metallic materials.



**Citation:** Wang, Y.; Wang, S.; Que, Z.; Fang, C.; Hashimoto, T.; Zhou, X.; Ramasse, Q.M.; Fan, Z. Manipulating Nucleation Potency of Substrates by Interfacial Segregation: An Overview. *Metals* **2022**, *12*, 1636. <https://doi.org/10.3390/met12101636>

Academic Editor: Angelo Fernando Padilha

Received: 12 August 2022

Accepted: 26 September 2022

Published: 29 September 2022

**Publisher's Note:** MDPI stays neutral with regard to jurisdictional claims in published maps and institutional affiliations.



**Copyright:** © 2022 by the authors. Licensee MDPI, Basel, Switzerland. This article is an open access article distributed under the terms and conditions of the Creative Commons Attribution (CC BY) license (<https://creativecommons.org/licenses/by/4.0/>).

**Keywords:** interfacial segregation; heterogeneous nucleation; grain refinement; solidification; electron microscopy

## 1. Introduction

A uniform solidification structure of fine and equiaxed grains is usually desirable for most engineering alloys, since it results in significant reduction of casting defects, leading to improved integrity and mechanical performance of the alloy castings [1–5]. Grain refinement of engineering alloys is usually achieved by inoculation through externally added grain refiners, which is common foundry practice in Al- and Mg- industries. The most widely used commercial grain refiners for Al alloys are Al-Ti-B based master alloys containing excess Ti (e.g., Al-3Ti-1B or Al-5Ti-1B), while Mg-Zr master alloy is the grain refiner commercially available for Mg alloys, although it is only effective for Al-free Mg alloys [3,6,7]. It has been well documented in the literature that promotion of the heterogeneous nucleation process by potent solid substrates, such as TiB<sub>2</sub> particles for Al- alloys and Zr for Mg- alloys, is an effective approach to achieving grain refinement, based on which a great deal of effort has been made over the last decades in the search for various

particles potent for nucleation; yet, in spite of these efforts, there has only been success to some degree.

During solidification, heterogeneous nucleation occurs on solid substrates (either endogenous or exogenous particles) present in an alloy melt, and nucleation potency of the substrates is dependent on the atomic arrangement in their surface plane [8]. As one of the important factors determining the nucleating potency, the lattice misfit at the interface between a substrate and nucleated new solid phase can be greatly modified by altering the atomic configuration of the substrate surface. In addition, our recent studies revealed that substrate surface roughness at atomic level [9] and chemical interaction between the substrate and the melt [10] affect nucleation potency considerably. Modification of atomic configuration and chemistry of substrate surface has been found to result in significant changes in nucleation potency. A good example is that, instead of  $\text{TiB}_2$  itself, an atomic layer of  $\text{Al}_3\text{Ti}$  2-dimensional compound (2DC) on the (0 0 0 1)  $\text{TiB}_2$  surface is actually responsible for the extremely high potency of the  $\text{TiB}_2$  particles for nucleation of  $\alpha\text{-Al}$  [11].

The addition of alloying elements usually promotes grain refinement by providing grain growth restriction, particularly helping to achieve columnar-to-equiaxed transition (CET) during solidification. The presence of alloying elements is, however, not always beneficial for grain refinement, because interaction between some elements and nucleation substrates could render the substrates impotent for heterogeneous nucleation, resulting in a coarse and columnar grain structure, i.e., the so-called “poisoning” effect. For instance, the presence of Zr [12–18] at a concentration of a few hundreds of ppm or high levels (>3.0%) of Si [19–25] in Al alloy melts results in a loss of grain refining ability of Al-Ti-B grain refiners. One of the current explanations for the poisoning effect is that the interaction between alloying elements and substrates leads to decrease in nucleation potency. Given the fact that alloying elements tend to segregate and react with the substrates at elevated temperatures during casting, it is essential to investigate the interactions and the resultant subsequences.

Our studies on metal/substrate (M/S) interfaces at atomic scale by the state-of-the-art aberration (Cs) corrected scanning transmission electron microscopy (STEM) and associated energy dispersive X-ray spectroscopy (EDS) and electron energy loss spectroscopy (EELS) have shown that segregation of alloying elements in Al- and Mg- alloy melts led to formation of various 2-dimensional compounds (2DCs) or 2-dimensional solutions (2DSs), depending upon the segregation behavior of the elements. For instance,  $\text{Al}_3\text{Ti}$  2DC [11] and  $\text{Ti}_2\text{Zr}$  2DC [26,27] at Al/ $\text{TiB}_2$ ,  $\text{Y}_2\text{O}_3$  2DC [28,29] at Mg/MgO, and Si-rich 2DS [30] at Al-Si/ $\text{TiB}_2$  interfaces have been identified at the various interfaces. Such interfacial segregations significantly affect nucleation potency of the substrates, resulting in either promoting or impeding the heterogeneous nucleation process during solidification. In this paper, we present an overview of the studies of the interfacial segregation behavior of various elements in Al and Mg alloys, the structure and chemistry of the segregation layers, and, particularly, the impacts of the segregation on subsequent heterogeneous nucleation and grain initiation processes. The advances we have made in understanding the mechanisms for grain refinement are presented, demonstrating the feasibility of manipulating heterogeneous nucleation by modifying the nucleation potency of a substrate through engineered interfacial segregation of desirable elements, achieving an effective control of grain structure of cast metallic materials.

## 2. Interfacial Segregation

### 2.1. Gibbs Adsorption Isotherm

The interfacial segregation in polycrystalline materials gives rise to a chemical heterogeneity, leading to interfacial regions having highly localized and altered chemistry. This may occur from either the equilibrium or the non-equilibrium partitioning of those solutes from solid solutions which are present as alloying elements or as residual impurities. Generally, equilibrium segregation at the interfaces describes distribution of solutes governed by minimization of total free energy of the systems: bulk plus interface [31]. Theoretically,

interfacial segregation is driven by reduction of interfacial energy and can be described by the Gibbs adsorption isotherm [32,33]. The Gibbs adsorption isotherm is usually used to elucidate the segregation phenomena at the surfaces or interfaces. It is based on the changes of surface or interfacial energy with the bulk activity of the solute [34]. For a dilute solution following Henry's law, the Gibbs adsorption isotherm can be written as [33,34]:

$$\Gamma_i = -\frac{1}{RT} \left[ \frac{d\gamma}{d \ln X_i} \right]_{T, P'} \quad (1)$$

where  $\Gamma_i$  is the surface or interfacial excess concentration of the solute with respect to its bulk composition,  $R$  is the universal gas constant,  $\gamma$  is the surface or interfacial energy at a given temperature  $T$ , and  $X_i$  is the mole fraction of the solute in the bulk. The Gibbs adsorption isotherm reveals that interfacial enrichment of a solute is directly related to the decrease in interfacial energy.

## 2.2. Segregation at Liquid/Substrate Interface

Solute segregation at the liquid/substrate interface in an alloy melt has been demonstrated to change both interfacial energies and the wetting behavior, and, therefore, affects heterogeneous nucleation behavior [35,36]. The thermodynamics of interfacial segregation of solute in an alloy melt has close analogy to monolayer gas adsorption at solid surfaces according to Gibbs adsorption isotherm and can be formalized in terms of the adsorption isotherm [32,33]. Applying the Gibbs adsorption isotherm, and using relevant approaches of thermodynamics and statistical mechanics, Men and Fan recently [37] developed an analytical model to describe the equilibrium solute segregation at the interface between metallic liquid (an A-B solution, where A is solvent and B is solute) and a solid substrate (N). Quantitatively, the saturated concentration of solute is determined by the equation below [37]:

$$\frac{X^i}{1-X^i} = \frac{X^l}{1-X^l} \exp \left\{ -\left[ a^i (\gamma_{BN}^i - \gamma_{AN}^i) - \frac{2\Omega}{Z} [Z_l(X^i - X^l) - Z_v(X^l - \frac{1}{2})] - T(\Delta S_A - \Delta S_B) \right] / RT \right\} \quad (2)$$

where  $X^i$  and  $X^l$  are the molar fractions of the solute atoms at the interface and in the bulk liquid, respectively,  $a^i$  is the interface area per mole atoms,  $\gamma_{AN}$  is the interfacial energy between solute A, and substrate and  $\gamma_{BN}$  is the interfacial energy between the solvent and the substrate,  $Z$  is the coordination number in the bulk melt,  $Z_l$  is the atomic coordination number in the interfacial layer,  $Z_v$  is the atomic coordination number to one of the adjacent layers.  $\Omega$  is the regular solution parameter, and  $\Delta S_A$  and  $\Delta S_B$  are change in entropy of solvent atoms and of solute atoms, respectively. Quantification using Equation (2) showed that the concentration of Ti at liquid Al-Ti/TiB<sub>2</sub> interface is significantly higher than that in the bulk melt, for instance, about 19 at.% in an Al-0.15 at.% Ti alloy melt at 660 °C. The analytical model shows that the interfacial solute segregation is governed by the following: (i) the difference in interfacial energies between the pure solute/substrate and pure solvent/substrate interfaces, (ii) the heat of mixing of the solution, and (iii) the difference in entropies of fusion between pure solute and solvent. This is useful for analyzing and quantifying interfaces in specific systems.

## 2.3. Approaches to Study of Interfacial Segregation

### 2.3.1. TEM/STEM Sample Preparation

The first challenge in examination of the interface between a nucleation substrate and matrix in a solidified alloy is the difficulty in preparing the samples which contain such substrate particles. In preparation of TEM specimens, for instance, assuming a particle of about 0.5  $\mu\text{m}$  in size had nucleated a grain which is typically 200  $\mu\text{m}$  in size, the probability of finding this particle inside the grain by 2D sectioning using the traditional metallography technique would be lower than one in a million, and an even lower probability of finding

this particle in the limited electron-transparent regions around the perforation of the  $\phi 3$  mm disc thin foil. This may be one of the reasons why there had been no success in observing the well-defined orientation relationships (ORs) by TEM to evidence nucleation in the history of Al-Ti-B master alloys until the mid-1990s, when Schumacher and Greer used devitrification of an Al-based metallic glass containing a high density of  $\text{TiB}_2$  particles as an analog to the nucleation of Al on  $\text{TiB}_2$ , and successfully obtained the first HRTEM images of the Al/ $\text{TiB}_2$  interface in this analog alloy [38,39].

A pressurized melt filtration technique was used in our research for collecting the substrate particles from the melt, and successful examination of substrate/metal interfaces by advanced electron microscopy has become a routine ever since [11]. In the melt filtration process, the prepared alloy melts containing either exogenously added or in-situ formed native solid particles was transferred into the crucible in the pressure chamber of the melt filtration unit. Argon was introduced to force the melt to flow through a porous ceramic filter attached to the bottom of the crucible. Substrate particles were, thus, collected in the region immediately above the filter. The solidified material above the filter, which contained the locally concentrated substrate particles, was subjected to sampling.

The filtration technique allows a significant increase in the number density of the substrate particle in a localized region, without changing either the particle potency or melt composition. This, particularly, greatly increases the probability of finding the particles in the TEM specimens. The technique has been successful in experimental studies of various substrate/metal interfaces, including Al/ $\text{TiB}_2$ , Mg/MgO, Al/ $\text{Mg}_2\text{O}_4$ , Al/ $\text{Al}_2\text{O}_3$  systems, etc., to reveal the mechanisms of heterogeneous, grain initiation and grain refinement, and Zr and Si poisoning [11,26–30,40,41]. More detailed description of the melt filtration for collection of solid particles from alloy melts and the reliability of the approach for nucleation studies can be found elsewhere [11,26,30,40,41].

### 2.3.2. Advanced Electron Microscopy

The state-of-the-art electron microscopy was performed to examine the collected substrate particles, with the focus being on their interfaces with the Al or Mg matrix. Scanning electron microscopy (SEM) was performed using a Carl Zeiss Crossbeam 340 microscope equipped with EDS. Thin foil specimens for TEM and STEM were prepared from 3 mm diameter discs sliced from the filtered residue material. The discs were manually ground to a thickness less than  $60 \mu\text{m}$  before further thinning by argon ion beam milling using a Gatan precision ion polishing system (PIPS) under a voltage of 1.0–5.0 kV and an incident beam angle of  $3\text{--}5^\circ$ . High resolution (HR) TEM examination was conducted on a JEOL 2100F microscope operated with an accelerating voltage of 200 kV. Atomic resolution STEM with Z contrast high-angle annular dark field (HAADF) imaging was carried out on an aberration (Cs)-corrected FEI Titan 80–200 instrument equipped with Super-X EDS system, operated with an accelerating voltage of 200 kV. High resolution elemental mapping by STEM/Super-X EDS was conducted to obtain compositional profiles across the Al/ $\text{TiB}_2$  interface.

Higher spacious and energy resolution in the STEM examinations was achieved using a dedicated STEM instrument, Nion UltraSTEM100, at the SuperSTEM Centre Laboratory UK. The microscope was operated at 100 kV acceleration voltage, with the probe forming optics configured for a 33 mrad convergence semi-angle. The microscope is equipped with Gatan EELS for chemical analysis. All high angle annular dark field (HAADF) STEM images were collected under image detector semi-angles of  $89\text{--}195$  mrad, and EELS collection semi-angles of 36 mrad. The chemical maps were created by integrating the signal above the relevant ionization edges over a suitable window, after removal of the continuous decaying background using a standard power law model, where the noise reduction was applied using principal component analysis.

In order to verify the experimental results obtained by high resolution (HR) -STEM, simulation of HAADF STEM images was conducted using the QSTEM multi-slice simulation package developed by Koch [42], with the inputs for the simulation being based

on the interfacial atomic configurations established from the experimental observations by HR-STEM.

### 2.3.3. Density Function Theory (DFT) Simulations

Parallel to the advanced microscopy, *ab initio* molecular dynamics (AIMD) simulations were carried out to investigate the elemental segregation at the interfaces and the atomic ordering of the liquid metal in the local areas close to the interfaces, with the simulation results being compared with the evidence obtained from TEM/STEM observations to verify the experimental results.

In the AIMD simulations, periodic conditions were employed and supercells were built for various systems of interfaces, such as L-Al/TiB<sub>2</sub>{0 0 0 1} and L-Al/ $\gamma$ -Al<sub>2</sub>O<sub>3</sub>{1 1 1} interfaces. For instance, hexagonal supercells with  $a_{SC} = 6 a_0$  and  $a_{SC} = 3\sqrt{3} a_0$  were built for L-Al/TiB<sub>2</sub>{0 0 0 1} interfaces where Ti and Zr segregated, respectively, and here  $a_0$  was the length of a-axis of TiB<sub>2</sub>. In this way, the inputs for the simulation were arranged with the atomic arrangements of the corresponding Ti or Zr atoms segregated at the interfaces according to the experimental observations. The lengths of the c-axis of the supercells were determined by the thickness of TiB<sub>2</sub>{0 0 0 1} slabs and the volumes of the liquids Al atoms. The built supercells contained 649 atoms and 830 atoms for the Ti- and Zr-segregated L-Al/TiB<sub>2</sub>{0 0 0 1} interfaces, respectively, based on the analysis of the interfacial interactions between the substrates and liquid Al.

Structural analysis in previous studies has revealed that, along its [0 0 1] orientation,  $\gamma$ -Al<sub>2</sub>O<sub>3</sub> (fcc structure with space group Fd-3m) has two different surfaces [43,44]. The constructed L-Al/ $\gamma$ -Al<sub>2</sub>O<sub>3</sub>{1 1 1} interfaces had a hexagonal supercell with  $a = \sqrt{2} a_0$ , where  $a_0$  was the lattice parameter of the  $\gamma$ -Al<sub>2</sub>O<sub>3</sub> phase at the simulation temperature [43,45]. Approximately one third of the terminating Al atoms were replaced by M (M is the segregation atom, e.g., Y or La) at the L-Al/ $\gamma$ -Al<sub>2</sub>O<sub>3</sub>{1 1 1} interfaces based on the experimental observations. The built supercells contained 310 atoms for the Y- or La- segregated L-Al/ $\gamma$ -Al<sub>2</sub>O<sub>3</sub>{1 1 1}, 649 atoms for the Ti segregated L-Al/TiB<sub>2</sub>{0 0 0 1} and 830 atoms for the Zr segregated L-Al/TiB<sub>2</sub>{0 0 0 1} based on the analysis of the interfacial interactions between the substrates and liquid Al. The large supercells helped avoid artificial nucleation of the liquid Al atoms, and statistically meaningful results were, therefore, obtained.

*Ab initio* molecular dynamics simulations were carried out using the code VASP (Vienna *ab initio* Simulation Package) [46], which employs the *ab initio* density functional theory (DFT) within the projector-augmented wave (PAW) framework [47]. The exchange and correlation terms were described using the generalized gradient approximation (GGA-PBE) [48]. A cut off energy of 320 eV and only  $\Gamma$ -point in the BZ [49] were used. Tests for cut-off energies from 250 eV to 400 eV showed that the present settings were reasonable.

The liquid Al was generated by equilibrating for about 10 picoseconds (ps) at 3000 K, followed by cooling down to and equilibration at a designated temperature for 10 ps. The liquid Al obtained in this way was brought into contact with the TiB<sub>2</sub> or  $\gamma$ -Al<sub>2</sub>O<sub>3</sub> substrate and, then, equilibrated at the same temperature for 10 ps to ensure equilibrium. The time-averaged method was employed to take samples with over several ps (2000–3000 steps, 1.5 fs/step) to satisfy the statistics [50–52].

### 2.3.4. Casting and Assessment of Grain Structure

Solidification structure of Al- and Mg- alloys was assessed using the standard TP-1 test method [53] which provides a cooling rate of  $\sim 3.5$  K/s at the central region of the transverse section 38 mm from the bottom of the TP-1 cast ingot. At a temperature of 50–100 K over the liquidus, alloy melts were prepared by melting the CP-Al or CP-Mg ingots with additions of the master alloys or elements, followed by holding at the temperature for 0.5–1 h before casting into the pre-heated TP-1 mold (350 °C), which was cooled by water spray.

Specimens for quantitative metallography of the solidified Al- and Mg- alloy TP-1 ingots were prepared following the standard grinding and polishing procedures. The preparation procedure of the Al alloy samples for optical microscopy was that, after

grinding by SiC abrasive papers and final polishing by SiO<sub>2</sub> suspension, the specimens were anodized in Barker's reagent (5 mL HBF<sub>4</sub> + 200 mL distilled water) under a voltage of 15–20 V for 1–2 min. Examination of grain structure and quantification of grain size were carried out in both the transverse and longitudinal sections of the solidified TP1 ingots under polarized light using a Zeiss optical microscope fitted with the Axio Vision 4.3 image analysis system.

### 3. Segregation at Al/TiB<sub>2</sub> Interface

#### 3.1. Nature of TiB<sub>2</sub> Particles

Figure 1a shows the morphology of TiB<sub>2</sub> particles in a commercial Al-5Ti-1B grain refiner master alloy, and Figure 1b is the statistical result of the particle size which fits a log-normal distribution with the size spreading over the range of 0.15 μm to 2.5 μm and with a geometrical mean of  $d_0 = 0.43 \mu\text{m}$  [54]. The faceted boride particles are typically of hexagonal shape, with the majority of the particles having a diameter/thickness ratio in the range of 3.1 to 5.6. The TEM image in Figure 2a confirms that the TiB<sub>2</sub> particles are faceted with their {0 0 0 1} basal and {1 1 0 0} prismatic planes [11], as shown schematically in Figure 2b. It has been well documented in the literature that heterogeneous nucleation of Al occurs on the basal surface of TiB<sub>2</sub>, where the (1 1 1)Al plane has the same hexagonal atomic arrangement to that of the basal plane of TiB<sub>2</sub>.

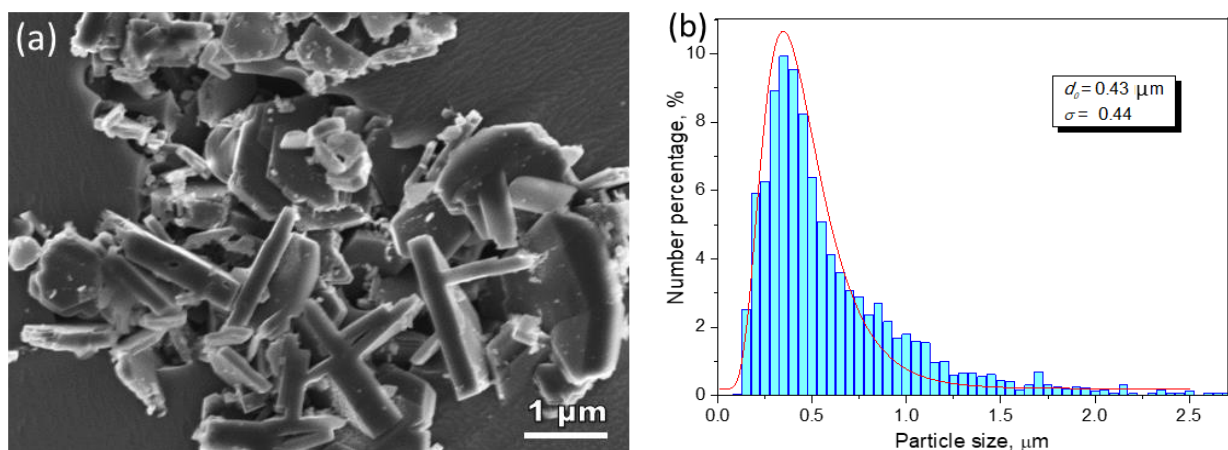


**Figure 1.** Nature of TiB<sub>2</sub> particles in commercial Al-5Ti-1B grain refiner [54]. (a) SEM image showing the typical hexagonal morphology; and (b) statistical analysis showing the log-normal size distribution with a geometrical mean of 0.43 μm and a standard deviation of 0.44. The grain refiner was supplied by LSM Co., Ltd.

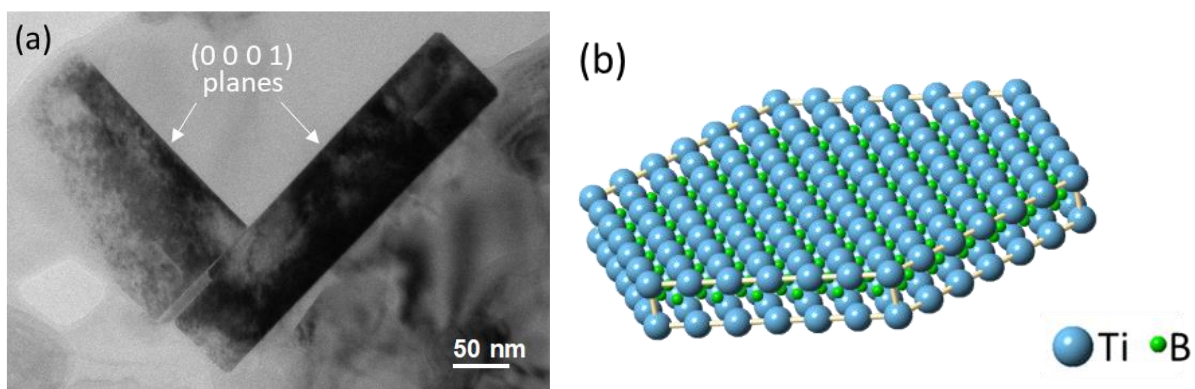


**Figure 2.** Surface termination and morphology of TiB<sub>2</sub> particles [11]. (a) TEM bright field image showing that the hexagonal TiB<sub>2</sub> particles are faceted with their {0 0 0 1} basal and {1 1 0 0} prismatic planes; and (b) 3D illustration showing schematically the atomic arrangement of TiB<sub>2</sub> crystal.

### 3.2. Al/TiB<sub>2</sub> Interface

Extensive TEM examination of multiple TiB<sub>2</sub> particles, which have clean surfaces without any elemental segregation, revealed that the majority of TiB<sub>2</sub> particles have no specific orientation relationship (OR) with the Al matrix. The high resolution TEM images in Figure 3a show an interface between Al and faceted (0 0 0 1) surface of a TiB<sub>2</sub> particle. It is seen that Al is away from any low index orientation while TiB<sub>2</sub> is in its [1 1  $\bar{2}$  0] direction. Despite a low possibility, Figure 3b confirms that heterogeneous nucleation of Al does occur on the TiB<sub>2</sub> particle surface, where the (1 1 1)<sub>Al</sub> and (0 0 0 1)<sub>TiB<sub>2</sub></sub> planes are paralleled to each other, with a deviation of 4.7 degrees between the [0  $\bar{1}$  1]<sub>Al</sub> and [1 1  $\bar{2}$  0]<sub>TiB<sub>2</sub></sub> directions. Therefore, the OR for “clean” (no interfacial segregation) TiB<sub>2</sub> and Al is:

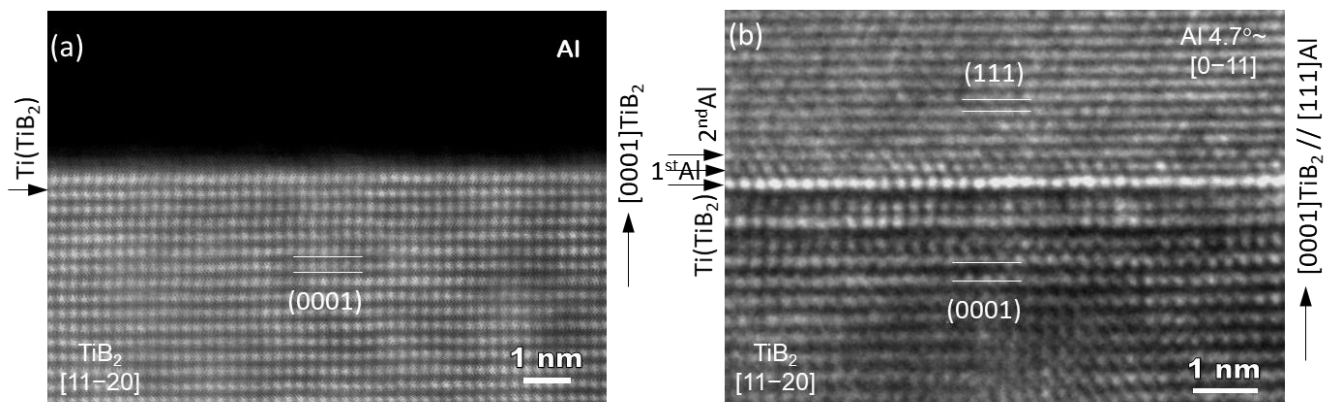


**Figure 3.** The interface between Al and a synthetic TiB<sub>2</sub> particle. HR-STEM images showing that (a) no particular orientation relationship (OR) between Al and TiB<sub>2</sub> and (b) (1 1 1)<sub>Al</sub> and (0 0 0 1)<sub>TiB<sub>2</sub></sub> planes are paralleled to each other and a deviation of 4.7° between [0  $\bar{1}$  1]<sub>Al</sub> and TiB<sub>2</sub> directions [55]. The OR is: (0 0 0 1)<sub>TiB<sub>2</sub></sub> // (1 1 1)<sub>Al</sub>, [1 1  $\bar{2}$  0]<sub>TiB<sub>2</sub></sub> 4.7° ~ [0  $\bar{1}$  1]<sub>Al</sub>. However, there is no such deviation between the first Al layer (as indicated) and the TiB<sub>2</sub>.

$$\text{OR1: } (0\ 0\ 0\ 1)_{\text{TiB}_2} // (1\ 1\ 1)_{\text{Al}}, \\ [1\ 1\ \bar{2}\ 0]_{\text{TiB}_2} \sim 4.7^\circ \text{ off } [0\ \bar{1}\ 1]_{\text{Al}}.$$

This is the direct experimental evidence to verify that clean a TiB<sub>2</sub> particle nucleates Al on its basal (0 0 0 1) surface. Theoretical work using molecular dynamics (MD) simulations by Fan et al. [55] recently demonstrated that, for a system with a negative lattice misfit, heterogeneous nucleation proceeds layer-by-layer, with the first layer accommodating the misfit through an edge dislocation network; the second layer twisting an angle through a partial screw dislocation network to reduce lattice distortion; and the third layer creating a crystal plane of the solid (the 2D nucleus) that templates further growth. The experimental TEM observation in Figure 3b confirms the theoretical prediction that the −4.22% misfit between Al and TiB<sub>2</sub> requires such an orientational deviation, except for the first atomic layer for the TiB<sub>2</sub> templated Al nucleation, i.e., a twist of the nucleated solid relative to the substrate.

In the practice of inoculation to achieve grain refinement of Al alloys in industry, TiB<sub>2</sub> particles are introduced to the alloy melt by addition of commercial Al-5Ti-1B master alloy prior to solidification. Similar to the case in Figure 3a, the majority of the added TiB<sub>2</sub> particles show no specific OR with Al. However, well-defined OR was observed between the two crystals. As shown by the high-resolution TEM image in Figure 4a, the crystal planes of (1 1 1)<sub>Al</sub> and (0 0 0 1)<sub>TiB<sub>2</sub></sub> are parallel to each other. Importantly, the directions of [0  $\bar{1}$  1]<sub>Al</sub> and [1 1  $\bar{2}$  0]<sub>TiB<sub>2</sub></sub> are perfectly parallel to each other with no deviation, as indicated by the corresponding selected area electron diffraction (SAED) pattern in

Figure 4b,c obtained from the area across the Al/TiB<sub>2</sub> interface. The OR for the TiB<sub>2</sub> from Al-5Ti-1B master alloy is thus identified as [11]:

$$\text{OR2} : (0\ 0\ 0\ 1)[1\ 1\ \bar{2}\ 0]_{\text{TiB}_2} // (1\ 1\ 1)[0\ \bar{1}\ 1]_{\text{Al}}$$

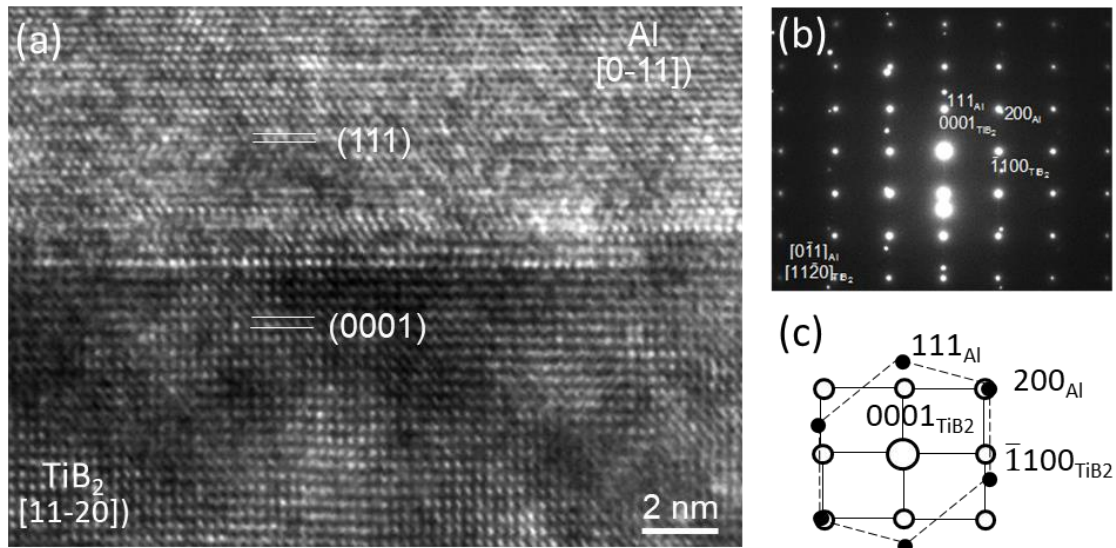


**Figure 4.** The interface between Al and TiB<sub>2</sub> from Al-5Ti-1B grain refiner [11]. (a) HR-TEM image showing the Al/TiB<sub>2</sub> interface viewed in the direction of [1 1  $\bar{2}$  0]<sub>TiB<sub>2</sub></sub> and [0  $\bar{1}$  1]<sub>Al</sub>; (b) selected area electron diffraction (SAED) pattern taken from TiB<sub>2</sub> and Al across the interface; and (c) the indexed pattern of (b). The orientation relationship (OR) between TiB<sub>2</sub> and Al is: (0 0 0 1)[1 1  $\bar{2}$  0]<sub>TiB<sub>2</sub></sub> // (1 1 1)[0  $\bar{1}$  1]<sub>Al</sub>.

By comparing Figures 3b and 4, it is noted that there is no deviation between [0  $\bar{1}$  1]<sub>Al</sub> and [1 1  $\bar{2}$  0]<sub>TiB<sub>2</sub></sub> directions for the TiB<sub>2</sub> from the grain refiner. This is attributed to Ti segregation at the Al/TiB<sub>2</sub> interface, leading to a reduced lattice misfit between Al and TiB<sub>2</sub> at the interface [11,55], which is further discussed in the next section.

OR2 indicates that, at the Al/TiB<sub>2</sub> interface, the most densely packed crystal planes with a hexagonal atomic arrangement of TiB<sub>2</sub> and  $\alpha$ -Al, i.e., (0 0 0 1)<sub>TiB<sub>2</sub></sub> and (1 1 1) <sub>$\alpha$ -Al</sub>, are matching each other, with their most-densely packed directions, i.e., [1 1  $\bar{2}$  0]<sub>TiB<sub>2</sub></sub> and [0  $\bar{1}$  1] <sub>$\alpha$ -Al</sub>, being parallel to each other. The fact that the majority of TiB<sub>2</sub> particles were far away from any particular OR with  $\alpha$ -Al indicates that most of the added boride particles did not contribute to the nucleation process, consistent with the conclusion derived from the free growth model, that only 0.1~1% of the added TiB<sub>2</sub> particles are active for heterogeneous nucleation [56].

Addition of Al-Ti-B grain refiners to Al alloy melts prior to solidification is a common practice in the Al industry, which gives castings a significant grain refinement with fully columnar-to-equiaxed transition (CET). As shown in Figure 5a,b, the grain structure of CP-Al solidified in the TP-1 mold changed dramatically from coarse columnar to fine equiaxed when 0.2% commercial Al-5Ti-1B grain refiner was added. The average size of  $\alpha$ -Al grains achieved with the inoculation by TiB<sub>2</sub> was quantified as  $175 \pm 16 \mu\text{m}$  [11], indicating the powerful grain refining effect of the grain refiner. However, additions of synthetic TiB<sub>2</sub> particles (Figure 5c), or the synthetic particles plus 56 ppm excess Ti (Figure 5d), where the size distribution and number density of the added synthetic TiB<sub>2</sub> particles and the excess Ti concentration were equivalent to those of the addition of 0.2% Al-5Ti-1B [11], showed no grain refining effect. A coarse and columnar grain structure resulted, although the width of the columnar grains appeared finer than those of the sample without addition of the particles. This demonstrates that synthetic TiB<sub>2</sub> particles do not have the ability to grain refine  $\alpha$ -Al, even combined with access to Ti in the melt [11]. The result from grain refinement tests and the absence of deviation in OR2 suggest that there is something



different between the synthetic  $\text{TiB}_2$  and those from the commercial Al-5Ti-1B grain refiner.

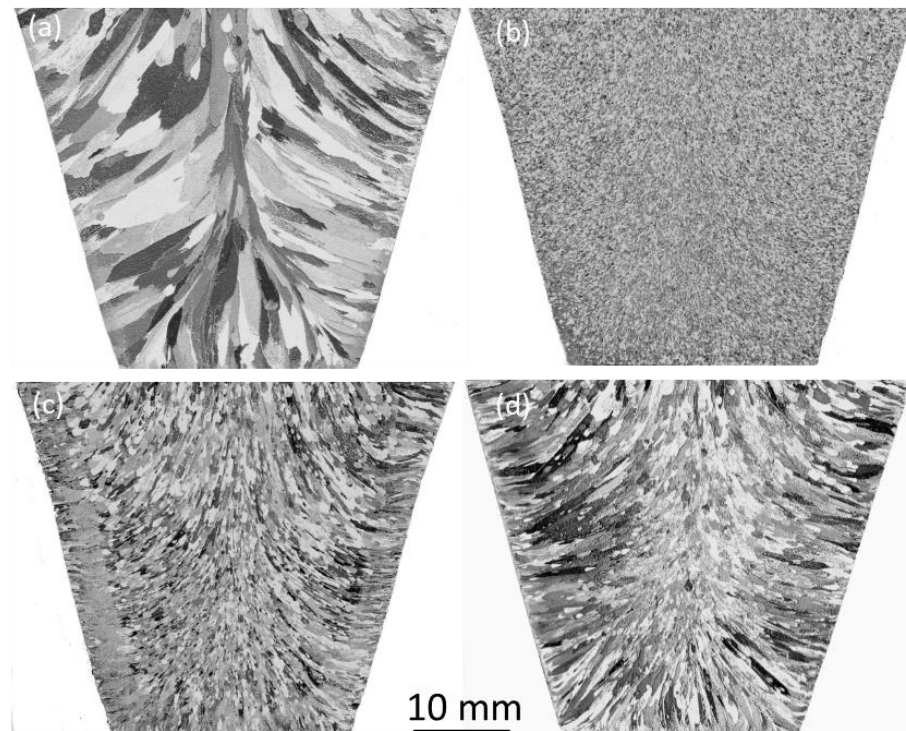


**Figure 5.** Grain structures of CP-Al solidified in TP-1 mold showing that synthetic  $\text{TiB}_2$  particles have no grain refining ability [11]. Macrographs of grain structures at longitudinal sections of CP-Al (a) without any addition; (b) with addition of 0.2% commercial Al-5Ti-1B grain refiner; (c) with addition of synthetic  $\text{TiB}_2$  particles; and (d) with both synthetic  $\text{TiB}_2$  and excess Ti ( $\text{TiB}_2$  numbers and excess Ti are equivalent to those of 0.2% Al-5Ti-1B).

### 3.3. Ti Segregation at Al/ $\text{TiB}_2$ Interface

The high resolution STEM HAADF image in Figure 6a shows the interface between Al and a  $\text{TiB}_2$  particles from the Al-5Ti-1B grain refiner, where the electron beam is along the  $[1\ 1\ \bar{2}\ 0]_{\text{TiB}_2}$  direction but off from any low-index zone axis of  $\alpha$ -Al. An atomic monolayer is clearly seen on the  $(0\ 0\ 0\ 1)$  surface of the  $\text{TiB}_2$ , with the spacing between the atomic monolayer and the surface  $(0\ 0\ 0\ 1)_{\text{TiB}_2}$  plane being measured as 0.25 nm, compared to 0.32 nm of the  $d$ -spacing of  $(0\ 0\ 0\ 1)_{\text{TiB}_2}$  planes [11]. SuperSTEM/EELS maps in Figure 6b–d reveal the chemical nature of the local region across the Al/ $\text{TiB}_2$  interface, confirming that the atomic monolayer contains Ti atoms [11]. According to the experimental evidence of structure and chemistry, and supported by results obtained by MD simulation [57], this Ti segregation layer was, therefore, identified as  $\text{Al}_3\text{Ti}$  2-dimensional compound (2DC) [11]. Figure 7a–c show schematically the atomic arrangement of  $(0\ 0\ 0\ 1)_{\text{TiB}_2}$ ,  $\text{Al}_3\text{Ti}$  2DC layer and  $(1\ 1\ 1)$  Al plane respectively, and the schematic in Figure 7d is the 3-dimensional construction of the monolayer on the  $(0\ 0\ 0\ 1)$  surface of  $\text{TiB}_2$ .

MD simulation was conducted by Qin and Fan to investigate the involvement of  $\text{Al}_3\text{Ti}$  in the heterogeneous nucleation of Al on  $\text{TiB}_2$  at an atomistic scale [57]. It was found that a two-dimensional  $\text{Al}_3\text{Ti}$  layer might remain on  $\text{TiB}_2$  at a temperature above the Al liquidus. The simulation results showed that this 2D  $\text{Al}_3\text{Ti}$  underwent interface reconstruction by forming a triangular pattern, which consisted of different alternative stacking sequences. The transition region between the triangles forms an area of strain concentration. Through this mechanism, the interfacial  $\text{Al}_3\text{Ti}$  layer stabilizes itself by localizing the large misfit strain between  $\text{TiB}_2$  and  $\text{Al}_3\text{Ti}$ .

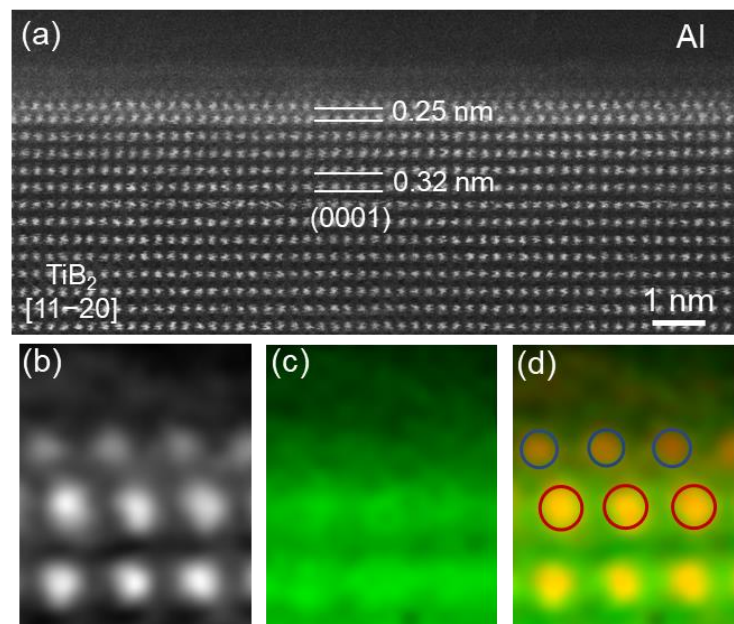


**Figure 6.** Segregation of Ti at Al/TiB<sub>2</sub> interface [11]. (a) Z-contrast STEM-HAADF image; (b) local Z-contrast HAADF image across the Al/TiB<sub>2</sub> interface; (c) atomic resolution EELS map of Ti K-edge; and (d) superimposition of the local image and Ti K-edge map. The atomic columns with blue circles are Ti atoms-rich columns, and those with red circles are Ti columns of TiB<sub>2</sub>. The atomic resolution EELS mapping confirms that the atomic monolayer at the interface contains Ti atoms.

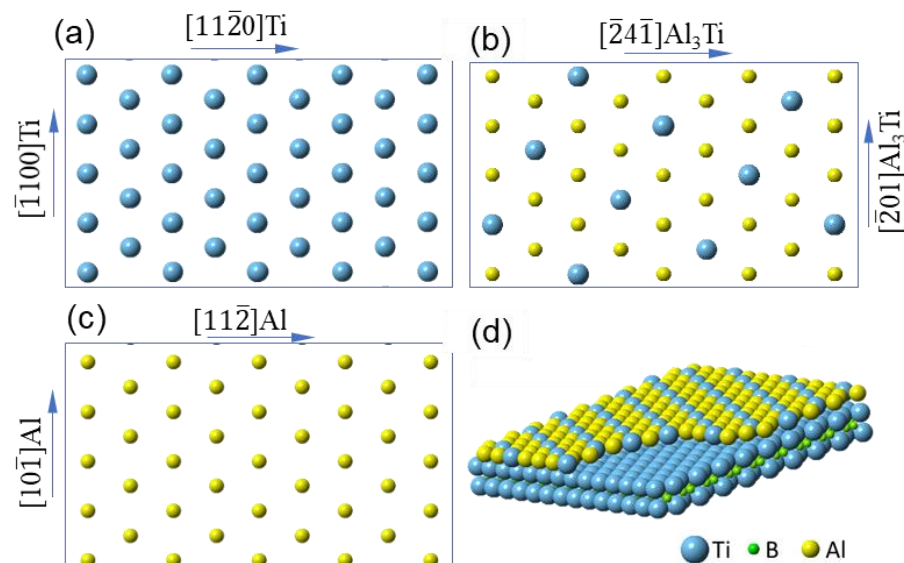


**Figure 7.** Atomic arrangement of the matching planes at the interface between Al, Al<sub>3</sub>Ti 2DC and TiB<sub>2</sub> [11]. Schematics showing (a) Ti atoms in (0 0 1)TiB<sub>2</sub> plane; (b) Ti and Al atoms in (1 1 2)Al<sub>3</sub>Ti plane; (c) Al atoms in (1 1 1)Al plane; and (d) 3D illustration of Al<sub>3</sub>Ti 2DC on the TiB<sub>2</sub> surface.

The heterogeneous nucleation behavior of Al on TiB<sub>2</sub>/Al<sub>3</sub>Ti substrates was analyzed by Wang et al. [58] using AIMD simulations. Structural ordering was clearly seen in the liquid close to the TiB<sub>2</sub> and Al<sub>3</sub>Ti substrates at temperatures below the Al melting point. They found that the Ti-terminated TiB<sub>2</sub> surface had greater potential to nucleate Al. In particular, they observed that, compared to the TiB<sub>2</sub> substrate, the ordering in liquid Al close to the (1 1 2) terminating surface of Al<sub>3</sub>Ti substrate was stronger on the Al<sub>3</sub>Ti substrate and that the liquid Al readily transformed into a solid fcc-like structure at a smaller undercooling. This verified the higher nucleation potency of Al<sub>3</sub>Ti over TiB<sub>2</sub>.

Simulations by Ma et al. [59] also revealed an almost fully ordered liquid Al layer on  $(0\ 0\ 0\ 1)\text{TiB}_2$  substrates.

The nucleation potency of a substrate is usually reflected, to a certain extent, by the lattice misfit at the interface between the substrate and the nucleated new solid phase at the moment of nucleation. According to OR2, the lattice misfit between Al and  $\text{TiB}_2$  at the interface is  $-4.22\%$  at  $660\text{ }^\circ\text{C}$ , and the misfit decreases to  $0.09\%$  when the  $\text{Al}_3\text{Ti}$  2DC layer is formed. This means that the formation of the  $\text{Al}_3\text{Ti}$  2DC on the  $\text{TiB}_2$  surface results in a significantly increased nucleation potency of  $\text{TiB}_2$  particles by the much-reduced absolute lattice misfit.

A bulk  $\text{Al}_3\text{Ti}$  phase is stable in an Al-Ti alloy melt only when Ti concentration is greater than  $0.15\%$  according to the Al-Ti equilibrium phase diagram. However,  $\text{Al}_3\text{Ti}$  2DC could be stable at the metal/substrate interface at a much lower Ti concentration of the bulk melt, driven by reduction of interfacial energy, due to Ti segregation according to Gibbs adsorption theorem, as shown by the theoretical analysis in [37]. This is the case of the present work where  $\text{Al}_3\text{Ti}$  2DC is readily observed on the  $(0\ 0\ 0\ 1)$  surface of  $\text{TiB}_2$  particles. Further experiment demonstrated that the  $\text{Al}_3\text{Ti}$  2DC layer could be deliberately formed on the surface of synthetic  $\text{TiB}_2$  particles by interfacial Ti segregation [11]. As shown in Figure 8a,b, the synthetic  $\text{TiB}_2$  particles treated by melt shearing in Al-Ti alloy melt for 10 min at  $850\text{ }^\circ\text{C}$  became highly effective in grain refining CP-Al (Figure 8b) [11], comparable to those in a commercial Al-5Ti-1B grain refiner (Figure 5b). However, the pre-existing  $\text{Al}_3\text{Ti}$  2DC could be dissolved from the  $\text{TiB}_2$  surface.  $\text{TiB}_2$  particles from a commercial Al-5Ti-1B grain refiner have been seen to have no grain refining ability after being held in a CP-Al melt at  $720\text{ }^\circ\text{C}$  for 78 h (Figure 8c) or treated in the CP-Al melt by high shear at the temperature for 45 min (Figure 8d), respectively [11]. The result verified that  $\text{Al}_3\text{Ti}$  2DC, instead of  $\text{TiB}_2$  itself, is responsible for the increased potency and, thus, the significant refining effectiveness of the commercial Al-5Ti-1B master alloys.

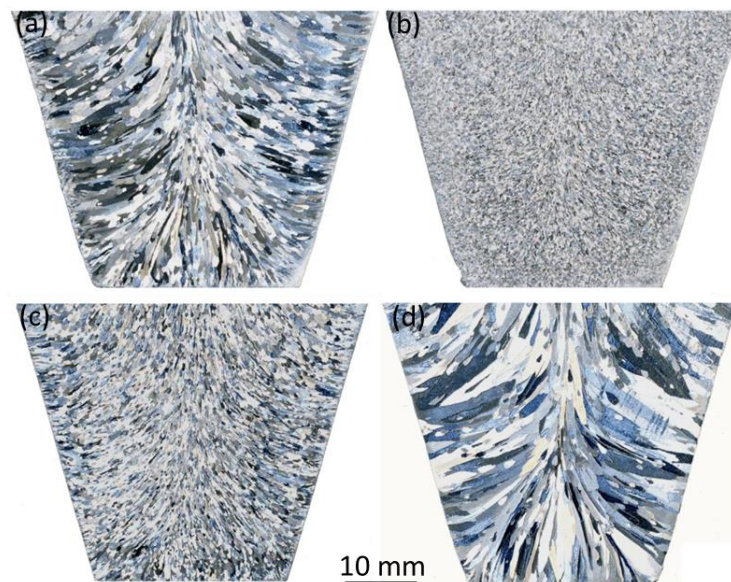


**Figure 8.** Grain structures of TP-1 cast CP-Al ingots reflecting the formation and dissolution of  $\text{Al}_3\text{Ti}$  2DC on  $\text{TiB}_2$  surface [11]. (a,b) With the addition of self-made Al-1Ti-0.2B master alloy (the excess Ti and  $\text{TiB}_2$  number density are equivalent to those of the addition of  $0.2\%$  Al-5Ti-1B grain refiner) from synthetic  $\text{TiB}_2$  particles in Al-Ti melt by intensive melt shearing at  $850\text{ }^\circ\text{C}$  for (a) 2 min and (b) 10 min, showing grain refinement in (b) (indicating the formation of  $\text{Al}_3\text{Ti}$  2DC on the synthetic  $\text{TiB}_2$  after melt shearing for 10 min); and (c,d) with addition of commercial Al-5Ti-1B grain refiner and then the melt was (c) held at  $720\text{ }^\circ\text{C}$  for 78 h or (d) treated by melt shearing for 45 min at  $720\text{ }^\circ\text{C}$ , showing no grain refinement (indicating dissolution of  $\text{Al}_3\text{Ti}$  2DC from  $\text{TiB}_2$  surface).

The difference between the  $\text{TiB}_2$  particles from commercial Al-Ti-B grain refiners and the synthetic ones is that the former have the  $\text{Al}_3\text{Ti}$  2DC layer on their surface, with the 2DC layer being readily formed at the high processing temperature and high excess Ti concentration during the production processes of the grain refiners.

Grain refinement of Al alloys achieved by addition of Al-5Ti-1B grain refiner is attributed to the factors below:

- (i) Formation of  $\text{Al}_3\text{Ti}$  2DC on the surface of  $\text{TiB}_2$  particles during the grain refiner production process, which significantly increased the potency of  $\text{TiB}_2$  for nucleation of  $\alpha\text{-Al}$ ;
- (ii) Sufficient numbers of added  $\text{TiB}_2$  particles which were coated with the  $\text{Al}_3\text{Ti}$  2DC layer, and suitable particle size and size distribution, which guaranteed sufficient number of grains to be initiated and grown from the nucleating  $\text{TiB}_2$  particles and achieved grain refinement;
- (iii) Excess Ti in the alloy melt after grain refiner addition generated growth restriction, which increased the effectiveness of the grain refiner by allowing more  $\text{TiB}_2$  particles to be active for heterogeneous nucleation, which, in turn, promoted the columnar-to-equiaxed transition.

### 3.4. Zr Segregation at Al/ $\text{TiB}_2$ Interface

Zr-containing Al- alloys are usually difficult to be grain refined by commercial Al-Ti-B grain refiners with standard addition rates [12–18]. Experiments have demonstrated that addition of Zr, even in a concentration of as low as a few hundred ppm, to Al alloy melts inoculated by Al-Ti-B grain refiner would result in no grain refinement after solidification [2,12,15]. The loss of grain refining ability for Al-Ti-B grain refiners caused by Zr addition is referred to as “Zr poisoning”. The refined grain structure (Figure 9a,c) of CP-Al by Al-5Ti-1B grain refiner is replaced by a coarse and columnar one (Figure 9b,d) when 0.0558% (558 ppm) Zr is added to the Al melt [26,27].

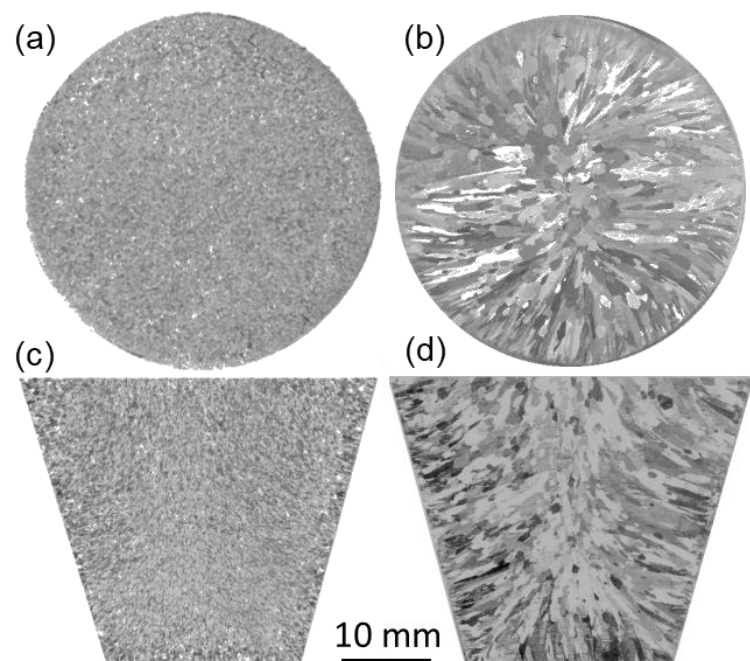


**Figure 9.** Grain structures of TP-1 cast CP-Al ingots showing Zr poisoning on Al-5Ti-1B grain refiner [26,27]. (a,c) With addition of 0.2% commercial Al-5Ti-1B grain refiner and (b,d) with additions of both 0.2% of the grain refiner and 558 ppm Zr, showing that the grain refiner lost its ability to grain refine CP-Al when the small amount of Zr was present in the melt. (a,b) Transverse and (c,d) longitudinal sections.

STEM examinations of  $\text{TiB}_2$  particles introduced to the Al-Zr alloy melts by addition of a commercial Al-5Ti-1B grain refiner were carried out to study the effect of Zr on  $\text{TiB}_2$  particles [26]. STEM HAADF image and the corresponding super-X EDS maps across the Al/ $\text{TiB}_2$  interface are shown in Figure 10, where Zr enrichment at the interface is clearly seen (Figure 10b), even at such a low Zr concentration (558 ppm). The Zr segregation corresponds to the brighter contrast of the interfacial layer seen in the HAADF image (Figure 10a). Figure 10c,d indicate that the main impurities in the alloy melt, Fe and Si, did not segregate at the interface.

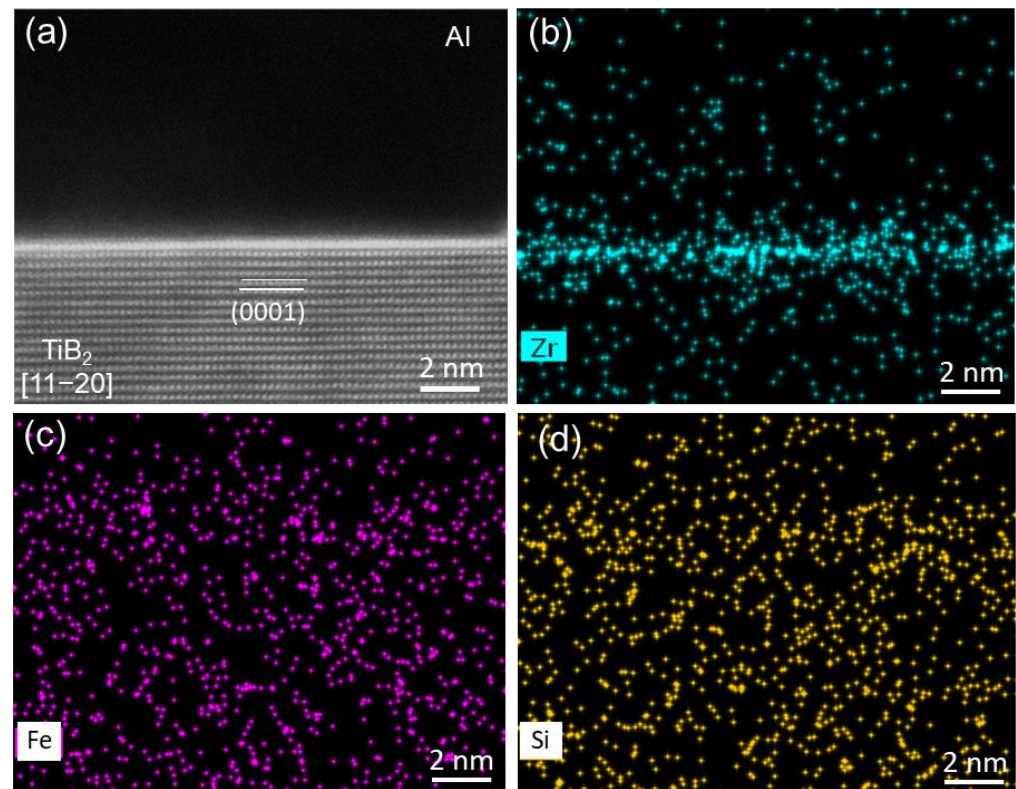


**Figure 10.** Zr segregation at Al/ $\text{TiB}_2$  interface [26]. (a) STEM-HAADF image across Al/ $\text{TiB}_2$  interface viewed along  $[1\ 1\ \bar{2}\ 0]\text{TiB}_2$  direction, and (b–d) super-X EDS elemental mapping of (b) Zr (cyan), (c) Fe (purple) and (d) Si (yellow) across the interface, showing Zr segregation but no segregation of Fe and Si at the interface.

STEM HAADF imaging at high magnifications reveals that the Zr interfacial segregation results in the formation of an atomic monolayer at the Al/(0 0 0 1) $\text{TiB}_2$  interface, with the atomic columns in the monolayer being brighter than the Ti columns in the (0 0 0 1) plane of  $\text{TiB}_2$ , as shown in Figure 11a, where the interface is viewed along  $[1\ 1\ \bar{2}\ 0]\text{TiB}_2$  direction [26]. The higher brightness of the atom columns verifies the presence of heavier Zr atoms (than Ti) in the monolayer. When viewed along  $[1\ 0\ \bar{1}\ 0]\text{TiB}_2$  direction, the brighter atomic columns of the monolayer appear in a periodic pattern, i.e., one bright column between two darker ones, as shown in Figure 11b. This suggests that, apart from Zr atoms, there is at least one type of other atom in the layer, with the in-plane atomic arrangement being ordered.

According to the experimental evidence of both structure and chemistry, the interfacial segregation layer is identified as  $\text{Ti}_2\text{Zr}$  2DC [26,60], with its in-plane atomic arrangement and 3D construction being shown schematically in Figure 12a,b, respectively. With the inputs derived from the atomic configuration of the  $\text{Ti}_2\text{Zr}$  2DC, HAADF image simulation was carried out using the QSTEM multi-slice package [42]. The simulation result in Figure 11c,d is in good agreement with the experimental images in Figure 11a,b along both  $[1\ 1\ \bar{2}\ 0]\text{TiB}_2$  and  $[1\ 0\ \bar{1}\ 0]\text{TiB}_2$  directions, validating the nature of the Zr segregation layer at

the interface. Formation of the  $\text{Ti}_2\text{Zr}$  2DC layer resulted from the substitution of one third of Ti atoms in the top (0 0 0 1) Ti plane of  $\text{TiB}_2$  by Zr atoms from the melt, which was possibly due to  $\text{ZrB}_2$  being thermodynamically more stable than  $\text{TiB}_2$ . However, further penetration of Zr atoms into the  $\text{TiB}_2$  crystal structure beyond the top (0 0 0 1) Ti plane is difficult due to the presence of the layer of B atoms beneath the  $\text{Ti}_2\text{Zr}$  2DC, which have strong covalent bonds between the B atoms. Formation of any bulk  $\text{ZrB}_2$  or  $(\text{Zr}_x\text{Ti}_{1-x})\text{B}_2$  are kinetically unfavorable, even if they are thermodynamically feasible, as suggested in the literature [12,61,62].

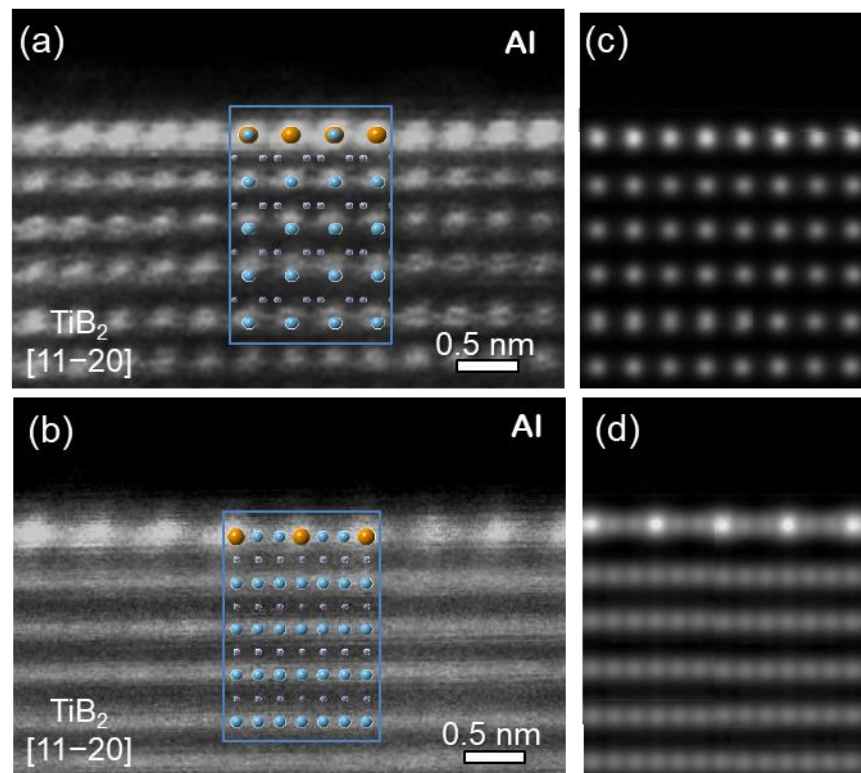


**Figure 11.** Formation of Zr segregation layer ( $\text{Ti}_2\text{Zr}$  2DC) at Al/ $\text{TiB}_2$  interface [26,27]. (a,b) STEM-HAADF images compared with (c,d) simulated ones in  $[1\ 1\ \bar{2}\ 0]\text{TiB}_2$  and  $[1\ 0\ \bar{1}\ 0]\text{TiB}_2$  direction, respectively. The simulation STEM HAADF images was carried out using the QSTEM multi-slice simulation package developed by Koch [42] according to the constructed super-lattice structure of  $\text{Ti}_2\text{Zr}$  2DC based the experimental HR-STEM observation.

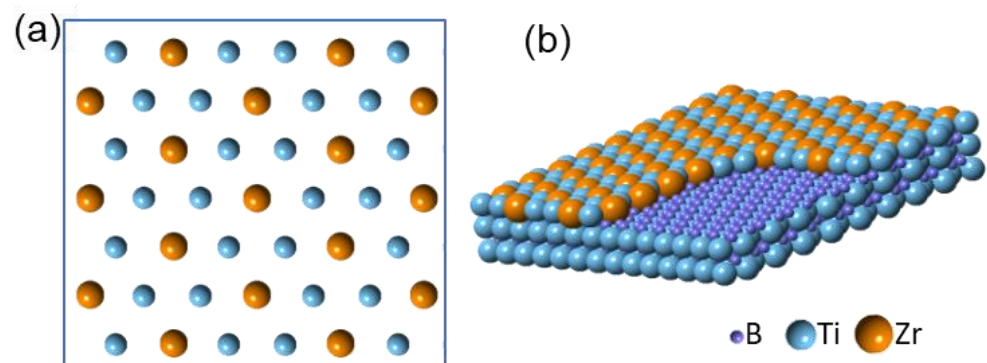


**Figure 12.** Crystal structure and chemistry of the Zr segregation monolayer ( $\text{Ti}_2\text{Zr}$  2DC) at Al/ $\text{TiB}_2$  interface [26]. (a) In-plane arrangement of Zr (larger orange spheres) and Ti (smaller blue spheres) atoms in the  $\text{Ti}_2\text{Zr}$  2DC layer and (b) 3D construction of the  $\text{Ti}_2\text{Zr}$  2DC on (0 0 0 1) $\text{TiB}_2$  surface.

Atomic ordering in the liquid Al adjacent to the  $\text{TiB}_2$  substrate at a temperature close to the alloy liquidus has been carried out by ab initio MD simulations (AIMD) for the  $\text{Al}(l)/\text{TiB}_2$  ( $\text{Ti}_2\text{Zr}$  2DC) system at 900 K, 1000 K and 1200 K, respectively [26]. Figure 13a shows the snapshot of the system equilibrated at 1000 K viewed along the  $[1\ 0\ \bar{1}\ 0]_{\text{TiB}_2}$  direction, and Figure 13b shows the atomic density profiles of the liquid Al adjacent to the  $\text{Al}(l)/\text{TiB}_2$  ( $\text{Ti}_2\text{Zr}$  2DC) interface equilibrated at the three different temperatures. It is clear from the experimental evidence in Figure 11 that the Zr atoms present in the  $\text{Ti}_2\text{Zr}$  2DC layer protrude into the liquid Al. This protrusion of Zr atoms is evident in the atomic density profile in Figure 13b where the peak for  $\text{Ti}_2\text{Zr}$  2DC is seen to be separated into two sub-peaks, marked as Ti and Zr. Quantified by the atomic density profile, the central positions of the Zr atoms in the 2DC layer were 0.45 Å away from that of the Ti atoms, which represents 19% of Al (1 1 1)  $d$ -spacing (0.2338 nm). This meant that the formation of  $\text{Ti}_2\text{Zr}$  2DC on the (0 0 0 1)  $\text{TiB}_2$  surface introduced a 19% atomic roughness to the  $\text{TiB}_2$  surface. The consequent effect of the 2DC formation was that the atomic ordering in the liquid Al adjacent to the L/S interface was significantly weakened; only two clear peaks are shown in the atomic density profile (Figure 13b), compared with 6 peaks on an atomically flat substrate surface [63]. In addition, the protrusion of Zr atoms in the  $\text{Ti}_2\text{Zr}$  2DC existed over a wide range of temperatures of 900 to 1200 K.

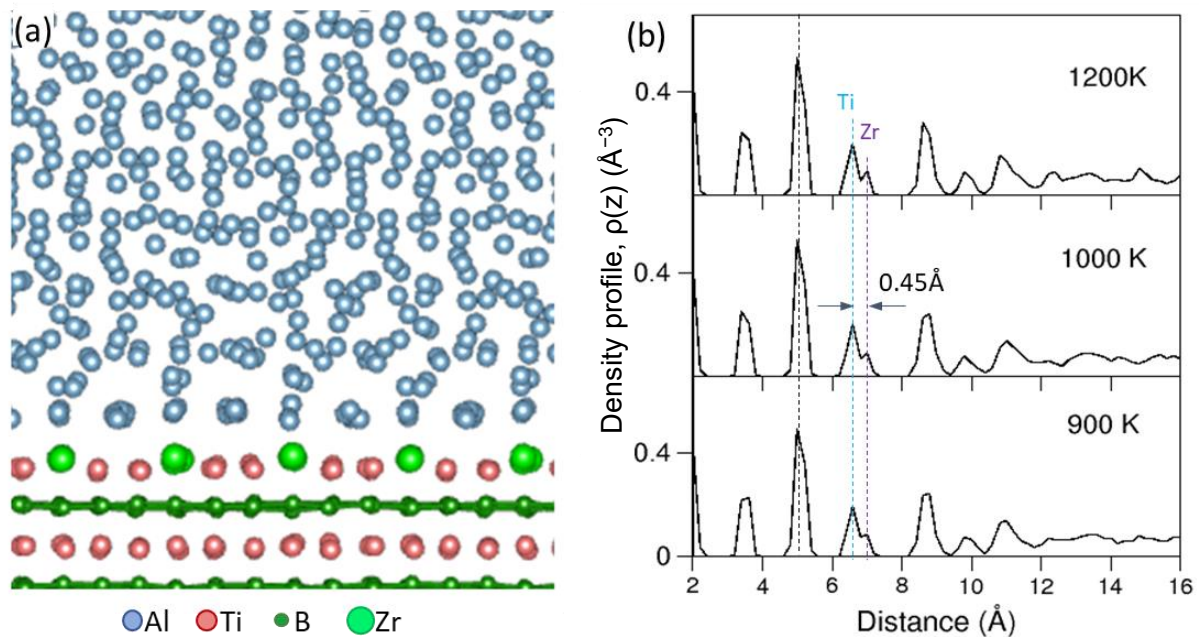


**Figure 13.** Ab initio MD simulation of Zr segregation at  $\text{Al}/\text{TiB}_2$  interface [26]. (a) Snapshot of  $\text{Al}(\text{liquid})/\text{TiB}_2(\text{Ti}_2\text{Zr}$  2DC) interface along  $[1\ 0\ \bar{1}\ 0]_{\text{TiB}_2}$  ( $\text{Ti}_2\text{Zr}$  2DC) direction simulated at 1000 K and (b) atomic density profiles  $\rho(z)$  across the  $\text{Al}(\text{liquid})/\text{TiB}_2$  ( $\text{Ti}_2\text{Zr}$  2DC) interface simulated at 900 K, 1000 K and 1200 K, respectively. The dotted lines in (b) indicate the position of the Ti and Zr atoms in the  $\text{Ti}_2\text{Zr}$  2DC.

With Zr being in Al alloy melts, the pre-existing  $\text{Al}_3\text{Ti}$  2DC on the  $\text{TiB}_2$  surface became thermodynamically unstable and dissolved. Due to the higher thermodynamic stability of  $\text{ZrB}_2$  than that of  $\text{TiB}_2$  [12,61], Zr atoms from the melt gradually substituted for some of the Ti atoms in the top (0 0 0 1)  $\text{TiB}_2$  plane and the  $\text{Ti}_2\text{Zr}$  2DC structure was, thus, formed. Figure 14 shows the on-going process of the  $\text{Ti}_2\text{Zr}$  2DC formation on the  $\text{TiB}_2$  surface, where the 2DC layer seen at the left-hand side would extend to cover the whole (0 0 0 1) surface of the  $\text{TiB}_2$  particle with proceeding of the segregation process [26].

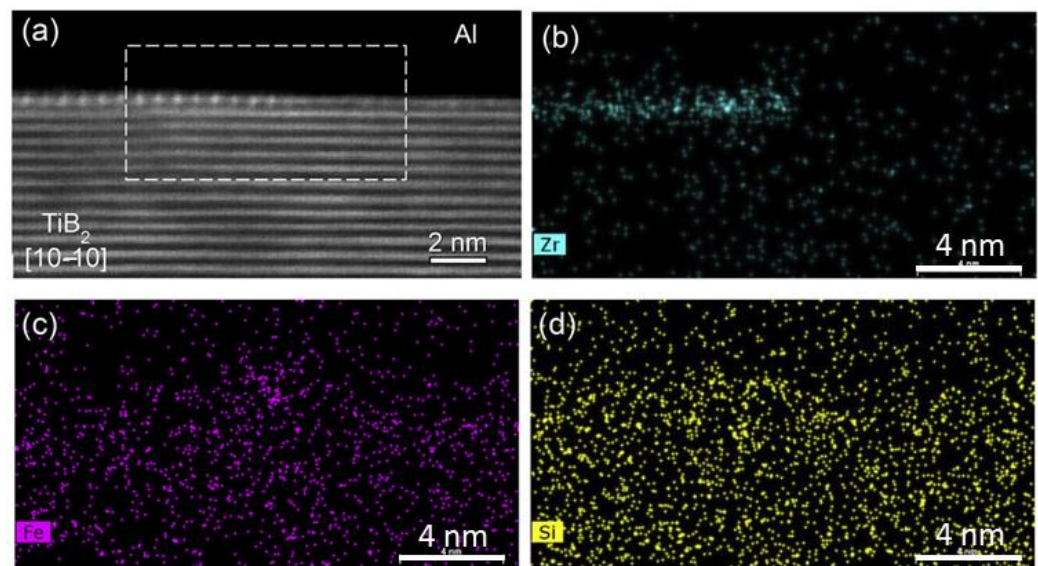


**Figure 14.** On-going of the Zr segregation process [26]. (a) STEM HAADF image across Al/TiB<sub>2</sub> interface viewed along [1 0  $\bar{1}$  0] TiB<sub>2</sub> direction, and (b–d) super-X EDS elemental mapping of (b) Zr, (c) Fe and (d) Si, showing the formation of Zr<sub>2</sub>Ti 2DC layer on the left-hand side, but not yet on the right-hand side of the (0 0 0 1) TiB<sub>2</sub> surface.

The Ti<sub>2</sub>Zr 2DC layer was coherent with (0 0 0 1) TiB<sub>2</sub> plane, so the lattice misfit between the 2DC layer and Al was back to the value of  $-4.22\%$ . The small lattice misfit  $0.09\%$  between Al<sub>3</sub>Ti 2DC and Al no longer existed. This would make the TiB<sub>2</sub> particles with Ti<sub>2</sub>Zr 2DC impotent for heterogeneous nucleation of  $\alpha$ -Al.

The spacing between Ti<sub>2</sub>Zr 2DC layer and the first (0 0 0 1) Ti plane was experimentally measured as  $0.34$  nm, larger than  $0.32$  nm of d-spacing of (0 0 0 1)Ti planes. As shown above, ab initio MD simulations performed for the Al(liquid)/TiB<sub>2</sub> (Ti<sub>2</sub>Zr 2DC) system revealed that the Zr atoms in Ti<sub>2</sub>Zr 2DC protruded into the liquid Al by  $0.45$  Å [26]. This meant that formation of Ti<sub>2</sub>Zr 2DC resulted in roughness at the atomic level on the TiB<sub>2</sub> surface. The simulation also demonstrated that, with such a large lattice misfit and atomically rough surface, the atomic ordering in the liquid Al adjacent to the Al(l)/TiB<sub>2</sub> interface was significantly weakened [26], indicating a great decrease in nucleation potency of the TiB<sub>2</sub> particles with Ti<sub>2</sub>Zr 2DC.

The mechanism underlying “Zr poisoning” of Al-Ti-B grain refiners is closely related to the dissolution of the pre-existing Al<sub>3</sub>Ti 2DC on the TiB<sub>2</sub> surface in the commercial Al-Ti-B based grain refiners and the formation of Ti<sub>2</sub>Zr 2DC in Al-Zr melt, rendering the TiB<sub>2</sub> particles impotent for heterogeneous nucleation of  $\alpha$ -Al. With addition of Zr to Al alloy melts, despite a concentration as low as a few hundred ppm, the Zr atoms tend to segregate at the TiB<sub>2</sub>/melt interface, resulting in the following effects: (i) dissolution of the pre-existed Al<sub>3</sub>Ti 2DC on the TiB<sub>2</sub> surface; (ii) the segregated Zr atoms at the interface substituting for some of the Ti atoms in the (0 0 0 1) surface to form the Ti<sub>2</sub>Zr 2DC atomic layer; and (iii) the Ti<sub>2</sub>Zr 2DC layer becoming atomically rough due to the considerably larger atomic size of Zr than that of Ti. The increased amplitude of lattice misfit (from  $0.09\%$  to  $4.22\%$ ) and atomically roughened particle surface render TiB particles impotent for heterogeneous nucleation and they are, thus, poisoned.

### 3.5. Si Segregation at Al/TiB<sub>2</sub> Interface

Si is also one of those elements which give rise to a poisoning effect on Al-Ti-B grain refiners. Experiments have shown that the Al-Ti-B based grain refiners are not effective for grain refining Al-Si alloys containing high Si concentrations [30]. As shown in Figure 15, the grain structure of Al-2.0Si alloy is refined by inoculation of  $0.2\%$  Al-5Ti-1B grain refiner with the average grain size being  $195 \pm 22$   $\mu\text{m}$ . However, the Al-8.4Si alloy added with



the same amount of the grain refiner shows a much coarser microstructure, with the average grain size being  $686 \pm 73 \mu\text{m}$ , although the grain structure remains equiaxed. The experimental results in previous studies agree that, when inoculated with Al-Ti-B grain refiners with usual addition rates (0.1~0.2%), the grain size of hypoeutectic Al-Si alloys decreases marginally with increasing Si concentration until about 2–3% and then it starts increasing with further increase in Si content, as shown by the representative data collected from the literature in Figure 16, plotted in Ref. [30].

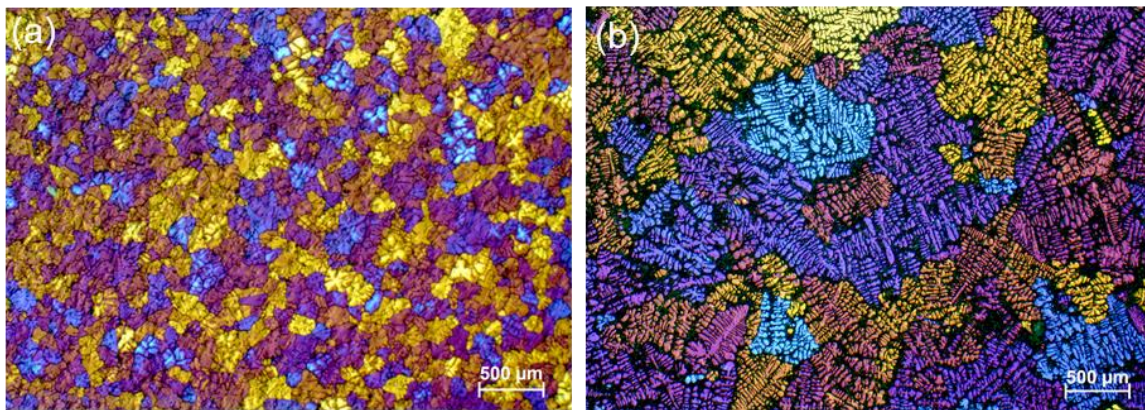


**Figure 15.** Si poisoning on Al-5Ti-1B grain refiner when its concentration is  $>3.0\%$  [30]. Optical micrographs showing microstructure of 0.2% Al-5Ti-1B inoculated (a) Al-2Si and (b) Al-8.4Si alloy solidified in TP-1 mold, showing the much coarser grain size of Al-8.4Si than that of Al-2Si.

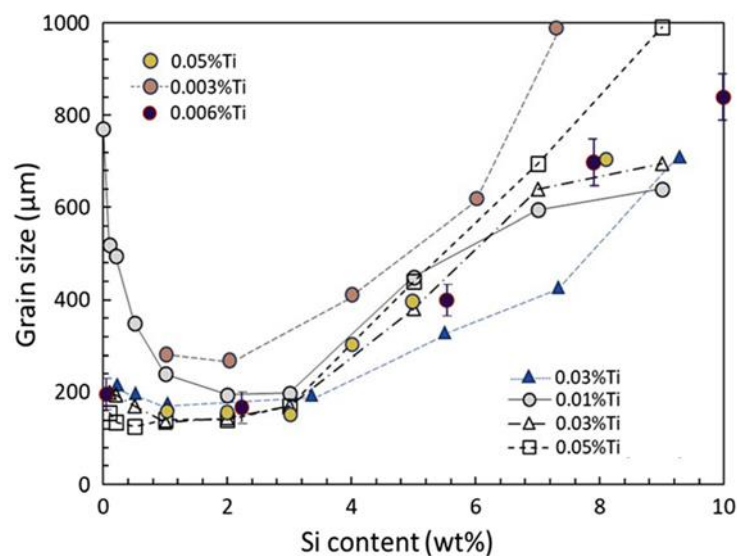


**Figure 16.** Grain size of binary Al-Si alloys (inoculated by Al-Ti-B grain refiner) as a function of Si concentration (the data were collected from the literature and plotted in Ref. [30]). The representative data collected from the literature showing the variation of the grain size with Si content of binary Al-Si alloys inoculated with Al-5Ti-1B grain refiner.

STEM/super-X EDS analysis on chemical profiles of the local region across the Al/TiB<sub>2</sub> interface reveals Si segregation at the interface [30]. As shown in Figure 17, a peak at the position of energy 1.74 keV, i.e., the characteristic K $\alpha$  peak of Si, is clearly seen in the EDS spectrum in Figure 17b, which was acquired from the Al/TiB<sub>2</sub> interfacial region, and the Si interfacial segregation is also shown in the corresponding EDS Si map in Figure 17c. Fe, as one of the main impurities in CP-Al, was not detected at the interface (Figure 17d). EDS analysis indicated that Si segregation at Al/TiB<sub>2</sub> interface was common to all the tested

TiB<sub>2</sub> particles collected from Al-Si alloys containing 2–10% Si and 0.2% Al-5Ti-1B grain refiner [30].

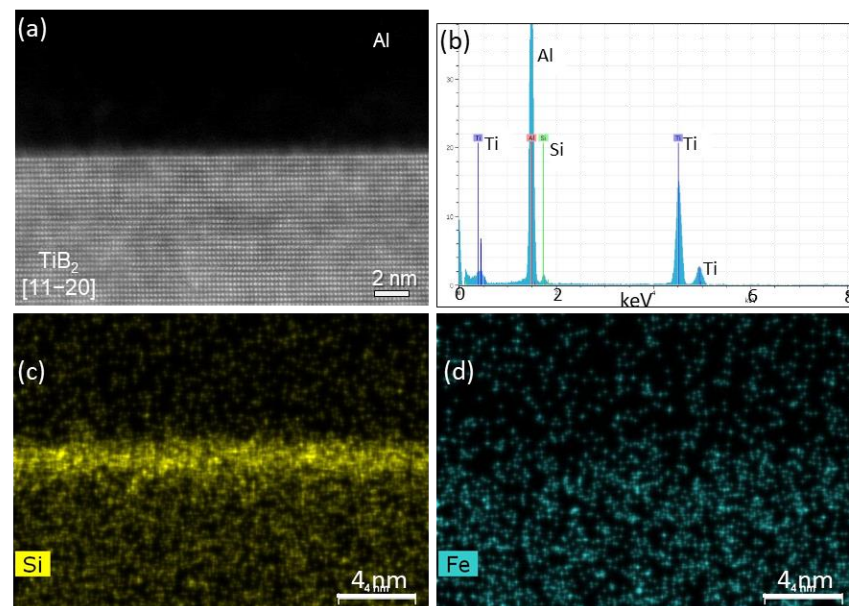


**Figure 17.** Si segregation at Al/TiB<sub>2</sub> interface data from [30]. (a) STEM-HAADF image of Al/TiB<sub>2</sub> interface for a TiB<sub>2</sub> particle from Al-8.4Si alloy containing 0.2% Al-5Ti-1B grain refiner; (b) Super-X EDS spectrum acquired from the interface; and (c,d) super-X EDS mapping of (c) Si and (d) Fe.

As shown earlier, TiB<sub>2</sub> particles in commercial Al-Ti-B grain refiners are covered by an Al<sub>3</sub>Ti 2DC layer on their surfaces due to Ti segregation and the 2DC layer is responsible for the powerful ability for grain refinement. However, high resolution STEM examinations of multiple TiB<sub>2</sub> particles which had been added to Al-Si alloy melts, revealed that the pre-existing Al<sub>3</sub>Ti 2DC on TiB<sub>2</sub> surface was missing. Figure 18 shows the Al/TiB<sub>2</sub> interface viewed from [1 1  $\bar{2}$  0]TiB<sub>2</sub> direction of a TiB<sub>2</sub> particle from Al-8.4Si alloy melt, where no extra atomic layer, other than the (0 0 0 1)Ti layer of TiB<sub>2</sub>, is seen, indicating the disappearance of the Al<sub>3</sub>Ti 2DC [30].

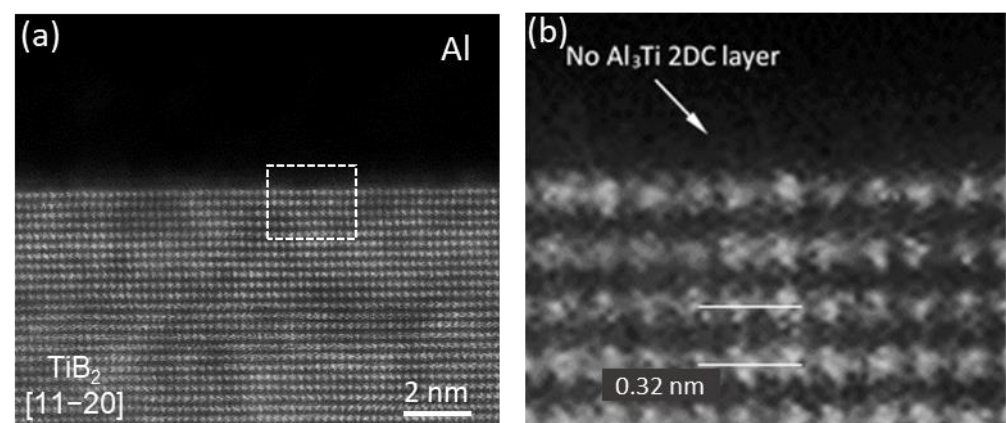


**Figure 18.** Disappearance of Al<sub>3</sub>Ti 2DC at Al/TiB<sub>2</sub> interface in Al-Si melt [30]. High resolution STEM-HAADF images of (a) Al/TiB<sub>2</sub> interface and (b) zoom of the marked local region across the interface viewed along [1 1  $\bar{2}$  0]TiB<sub>2</sub> direction for a TiB<sub>2</sub> particle (by addition of Al-5Ti-1B grain refiner) in Al-8.4Si alloy melt, showing that the pre-existing Al<sub>3</sub>Ti 2DC layer on the (0 0 0 1)TiB<sub>2</sub> surface is no longer there.

It is believed that, when TiB<sub>2</sub> particles are added to Al-Si melt, the Al<sub>3</sub>Ti 2DC on their surface is not stable and dissolves into the melt. Evidence of such dissolution was

experimentally observed in Al-Si alloys with a low Si concentration. Figure 19 shows the on-going dissolution of  $\text{Al}_3\text{Ti}$  2DC where the 2DC layer remained on the left-hand side but was missing on the right-hand side of the (0 0 0 1)  $\text{TiB}_2$  surface. The remainder of the 2DC layer was more readily observed in low Si Al-Si alloys than in high Si ones, indicating that  $\text{Al}_3\text{Ti}$  2DC was more unstable thermodynamically and kinetically, and, thus, dissolved faster in a high Si Al-Si melt than in a lower Si Al-Si melt [30].

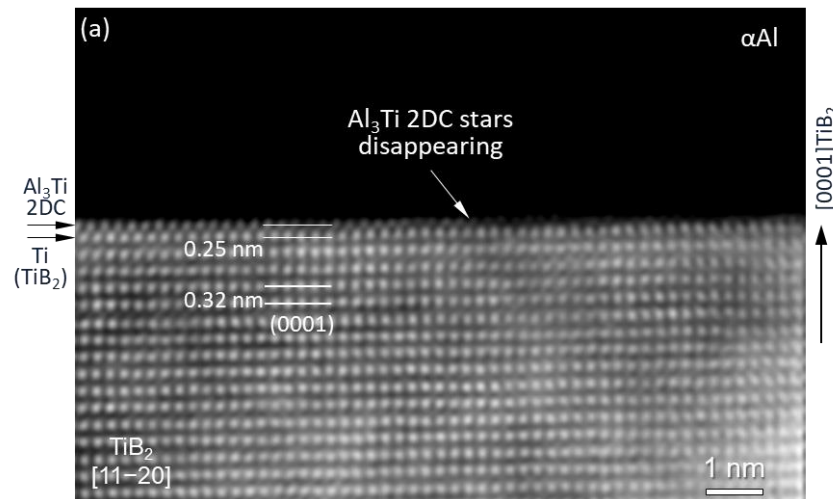


**Figure 19.** On-going of the dissolution process of  $\text{Al}_3\text{Ti}$  2DC at Al/ $\text{TiB}_2$  interface [30]. High resolution STEM HAADF image of the Al/ $\text{TiB}_2$  interface viewed along  $[1\ 1\ \bar{2}\ 0]$   $\text{TiB}_2$  direction, showing the remaining  $\text{Al}_3\text{Ti}$  2DC layer on the left-hand side of the (0 0 0 1) surface of  $\text{TiB}_2$  particle added to Al-2Si alloy melt.

Si segregation does not lead to the formation of any 2DC layer or 3D bulk phase at the Al/ $\text{TiB}_2$  interface. According to the Gibbs adsorption isotherm, solute segregation driven by interfacial energy reduction occurs only in one or two atomic layers. It is believed that Si enrichment by segregation at the interface can be considered a 2-dimensional solution (2DS), different from the cases of segregation of Ti or Zr, where in-plane ordered  $\text{Al}_3\text{Ti}$  2DC [11] or  $\text{Ti}_2\text{Zr}$  2DC [26] resulted at the Al/ $\text{TiB}_2$  interface, respectively.

Dissolution of  $\text{Al}_3\text{Ti}$  2DC due to Si segregation results in the reduced nucleation potency of  $\text{TiB}_2$ . As shown earlier, nucleation of  $\alpha$ -Al now takes place directly on the (0 0 0 1) surface of  $\text{TiB}_2$  with a much increased lattice misfit  $-4.22\%$  between  $\{0\ 0\ 0\ 1\}\text{TiB}_2$  and  $\{1\ 1\ 1\}\text{Al}$  instead of the small value  $0.09\%$  between  $\text{Al}_3\text{Ti}$  2DC and  $\{1\ 1\ 1\}\text{Al}$  at the interface. The mechanism for Si poisoning is, therefore, identified as.

1. Si interfacial segregation leads to enrichment of Si at the Al-Si melt/ $\text{TiB}_2$  interface. The higher the Si concentration in the melt, the more Si enrichment at the interface there is.
2. Si segregation at the Al-Si/ $\text{TiB}_2$  melt interface makes the pre-existed  $\text{Al}_3\text{Ti}$  2DC layer unstable on the  $\text{TiB}_2$  surface, and, thus, the 2DC dissolves gradually, resulting in a greatly decreased nucleation potency for the  $\text{TiB}_2$  particles. The dissolution rate of the 2DC layer increases with increasing Si enrichment at the interface.
3. The subsequence of the 2DC dissolution is a reduced total number of potent  $\text{TiB}_2$  particles available for heterogeneous nucleation and grain initiation of  $\alpha$ -Al, and, hence, an increased grain size.

### 3.6. Fe Segregation at Al/ $\text{TiB}_2$ Interface

Fe segregation has not been observed at the Al/ $\text{TiB}_2$  interface when its concentration is in an impurity level, e.g.,  $\sim 0.08\%$  in a commercial purity (99.8%) Al [26,30]. However, Fe readily segregates at the interface when a relatively high Fe concentration, e.g., a few percent, is present in Al melt [64–67]. Figure 20 shows Fe segregation at Al/ $(1\ 1\ 0\ 0)\text{TiB}_2$  ( $\text{AlB}_2$ )

interface in a sample in which the boride particles were in-situ synthesized by reaction of Al-8Fe and Al-10Ti master alloys in the CP-Al melt at 920 °C. Figure 20a shows that a Fe-rich interfacial segregation layer on the prismatic surface of  $\text{TiB}_2$  formed in a zig-zag fashion when viewed along  $[1\ 1\ \bar{2}\ 0]_{\text{TiB}_2}$  direction, with its atomic arrangement being schematically illustrated in Figure 20b. The EDS mapping in Figure 20d across the interface region in Figure 20c confirmed the Fe segregation at the interface. Interestingly, no Fe segregation was on the  $\{0\ 0\ 0\ 1\}$  basal surface of  $\text{TiB}_2$ .

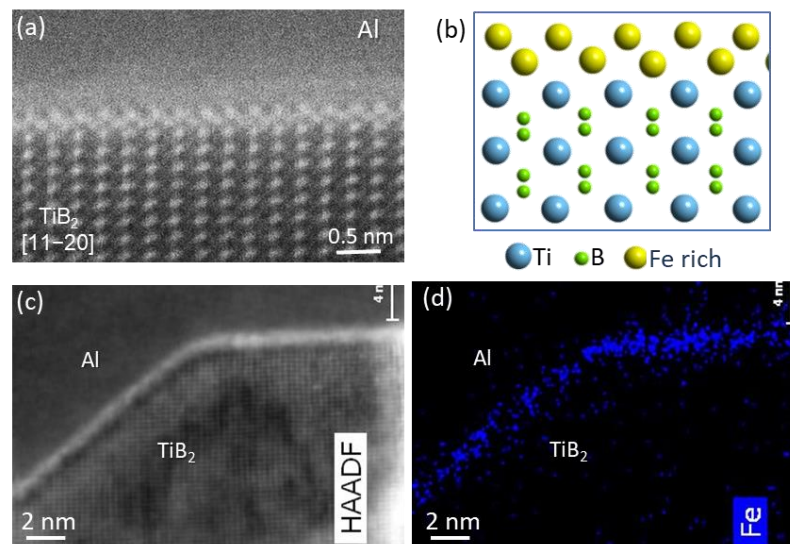


**Figure 20.** Fe segregation at the Al/(1 1 0 0) $\text{TiB}_2$  ( $\text{AlB}_2$ ) interface [64–66]. (a) High resolution STEM HAADF image showing the extra atomic layers at the interface when viewed from  $[1\ 1\ \bar{2}\ 0]_{\text{TiB}_2}$  direction; (b) schematic showing the zig-zag atomic arrangement of the interfacial layers viewed along the direction; and (c) STEM HAADF image and (d) superX-EDS mapping confirming the enrichment of Fe at the interface.

The behavior of Fe segregating selectively only on prismatic  $\text{TiB}_2$  surfaces has been repeatedly observed, as shown in Figure 21, with Fe segregation occurring discontinuously on the prismatic surface, but Si segregation covering both basal and prismatic surfaces of  $\text{TiB}_2$ . Interestingly, accompanied by Si segregation, there are two atomic layers in the regions where Fe is enriched when observed in  $[1\ 1\ \bar{2}\ 0]_{\text{TiB}_2}$  direction.

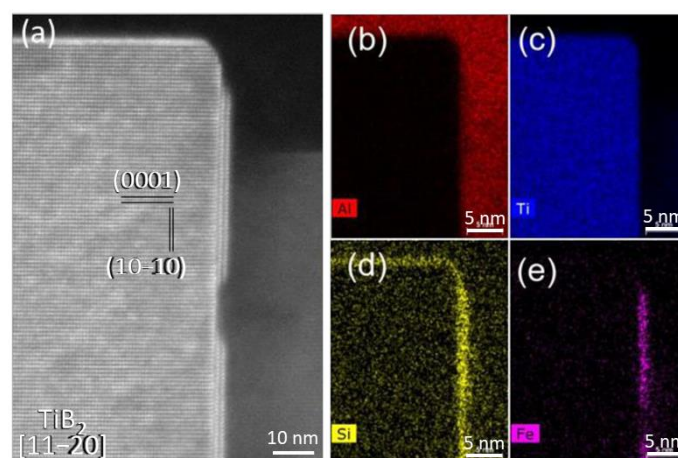


**Figure 21.** Segregation of Fe and Si at Al/ $\text{TiB}_2$  interface [64,68]. (a) High resolution STEM HAADF image across Al/ $\text{TiB}_2$  interface viewed along  $[1\ 1\ \bar{2}\ 0]_{\text{TiB}_2}$  direction; (b–e) super-X EDS elemental mapping of (b) Al, (c) Ti, (d) Si, and (e) Fe showing that Si segregates on all surface of  $\text{TiB}_2$  but Fe segregates only on  $(1\ 0\ \bar{1}\ 0)$  prismatic surface of  $\text{TiB}_2$ .

It has been demonstrated that  $\text{TiB}_2$  particles with Fe and Si segregation are effective to refine the primary  $\alpha\text{-Al}_{15}(\text{Fe,Mn})_3\text{Si}_2$  intermetallic phase in Al-Fe-Si-Mn alloys, with the size of the intermetallic phase being reduced from a few tens of micrometers to a few of micrometers [64–68]. The Fe- and Si-coated  $\text{TiB}_2$  particles are frequently found inside the primary  $\alpha\text{-Al}_{15}(\text{Fe,Mn})_3\text{Si}_2$  phase particles and have specific orientation relationships with the intermetallic phase, suggesting that more of such  $\text{TiB}_2$  particles participated in nucleation of the Fe-rich intermetallic compounds [65–68]. This is because, in addition to a structural templating, an extra compositional templating is provided by segregation of Fe and Si, and, thus, the heterogeneous nucleation and grain initiation processes are enhanced for the intermetallic compounds [64,68].

### 3.7. Cu Segregation at Al/ $\text{TiB}_2$ Interface

Cu is readily observed to segregate at the Al/ $\text{TiB}_2$  interface. The STEM HAADF images in Figure 22 show the interface between Al and both the (0 0 0 1) basal and (1 1 0 0) prismatic surfaces of a  $\text{TiB}_2$  particle from an Al-3Ti-1B-4.2Cu alloy. A brighter layer is visible at the (0 0 0 1) $\text{TiB}_2$  surface, indicating the segregation of the heavier (than Ti) Cu atoms on the (0 0 0 1) basal surface of  $\text{TiB}_2$ . As shown in Figure 22a, Cu seems not to segregate on the prismatic surface of  $\text{TiB}_2$ .

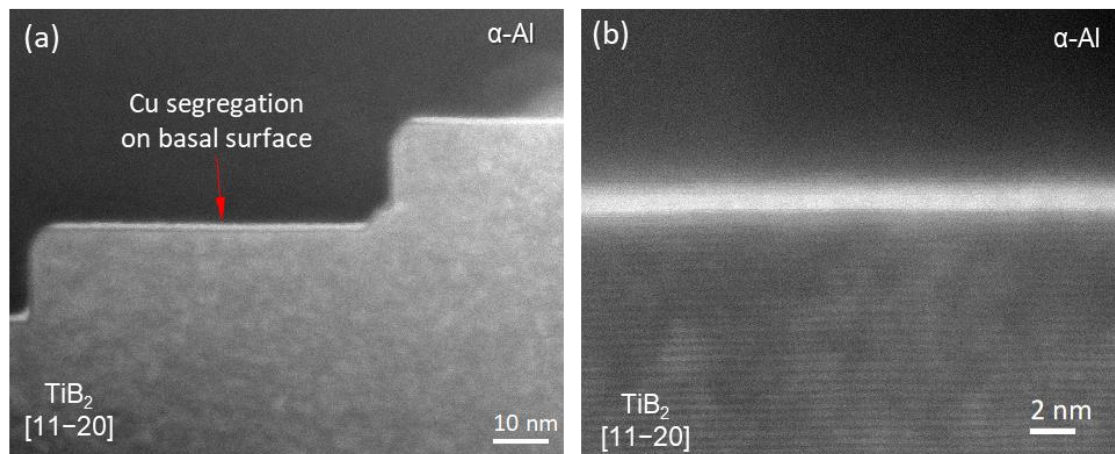


**Figure 22.** Cu segregation at Al/ $\text{TiB}_2$  interface. STEM HAADF images show (a) general view and (b) local region across the Al/ $\text{TiB}_2$  interface for a  $\text{TiB}_2$  particle in Al-3Ti-1B-4.2Cu alloy, where a bright segregation layer is visible on the (0 0 0 1) $\text{TiB}_2$  basal surface but not on the (1 1 0 0) prismatic surface of the  $\text{TiB}_2$ .

In an Al-3.5Cu alloy containing  $\text{TiB}_2$  particles which had been introduced by addition of commercial Al-5Ti-1B master alloy, Li et al. [69] observed that there was a Cu-rich layer about 2 nm thick covering both the basal and prismatic plane surfaces of  $\text{TiB}_2$  particles. It was further revealed that, on top of the (0 0 0 1) basal plane surface of  $\text{TiB}_2$ , there was an Al and Ti rich region which was an  $\text{Al}_3\text{Ti}$  2DC layer, followed by an Al-rich layer with a much lower Ti content, and, finally, a Cu-rich layer of about several atomic planes (2–3 atoms) thick which exhibited in-plane ordering. On the {1 1 0 0} prismatic surface of  $\text{TiB}_2$ , Cu segregation was also detected, although no  $\text{Al}_3\text{Ti}$  2DC layer was observed. The observation of an  $\text{Al}_3\text{Ti}$  2DC layer on the  $\text{TiB}_2$  surface was in agreement with our earlier work, with the 2DC layer being formed during the production of the commercial Al-5Ti-1B grain refiner.

It has been seen that segregation of Zr or Si results in dissolution of the pre-existed  $\text{Al}_3\text{Ti}$  2DC layer. However, Cu segregation apparently does not interfere with the pre-existing  $\text{Al}_3\text{Ti}$  2DC layer at the Al/ $\text{TiB}_2$  interface. Instead, the Cu-rich layer resulting from interfacial segregation was on the top of the  $\text{Al}_3\text{Ti}$  2DC [69]. Consequently, such a Cu-rich layer at the interface is expected to affect heterogeneous nucleation, although the actual effect has yet to be determined.

#### 4. Segregation at Mg/MgO Interface

##### 4.1. Nature of Native MgO Particles in Mg Alloy Melt

Magnesium oxide (MgO) is readily formed in-situ during heating and melting of Mg alloys due to the very high affinity of Mg with oxygen. The native MgO in Mg alloy melts are usually in the form of films that consist of numerous nano-sized MgO particles [28,40,41,70,71]. The oxide films in Mg alloy melts can be dispersed by means of intensive physical stirring; high shear, for instance, resulting in more discrete particles. Figure 23 gives such an example where the high shear imposed to the melt is demonstrated to disperse the oxide films in Mg-9Al alloy (Figure 23a) and commercial purity Mg (Figure 23b) and makes the MgO particles uniformly distribute in the melt (Figure 23c,d) [40,41,70,71]. The individual MgO particles are faceted with either {1 1 1} or {1 0 0} planes, being the terminating surfaces, displaying two distinctive morphologies, i.e., {1 1 1} terminated octahedral (Figure 24a) and {1 0 0} terminated cubic (Figure 24b). The size of the MgO particles follows the log-normal distribution, with the average size being about 70–80 nm [70,71].

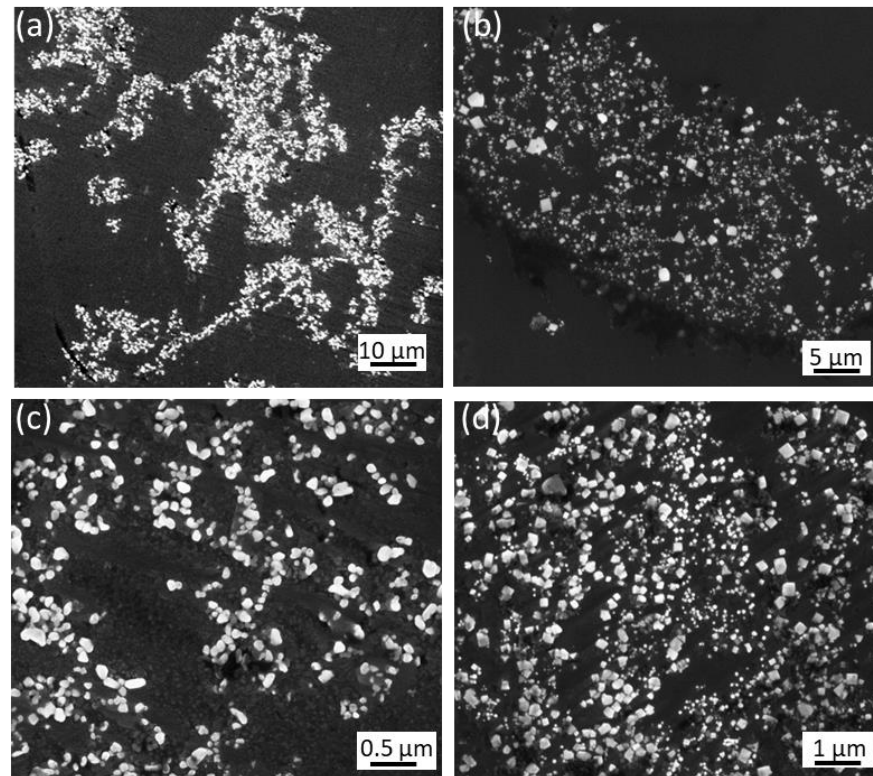


**Figure 23.** Morphology of MgO films and MgO particles [70]. SEM images showing general morphology of (a,b) native MgO films and (c,d) native MgO particles dispersed by melt shearing collected from (a,c) Mg-9Al and (b,d) commercial purity Mg melt. The oxide films are liquid films that contain numerous discrete MgO particles.

##### 4.2. MgO Acting as Nucleation Substrate

Native MgO has been demonstrated to act as an efficient substrate for nucleation of Mg, leading to significant grain refinement and improved mechanical properties for various Mg alloys [40,41,71–80]. Our experimental and theoretical investigations have shown that the key factors for native MgO to achieve grain refinement are its relatively poor nucleation potency and availability of high number density in the melt. The low nucleation potency of MgO enables a large nucleation undercooling  $\Delta T_n$  which is required for triggering a so-called explosive grain initiation (EGI) scheme [74,80] and the latter ensures numerous solid grains initiate and grow. MgO has a poor lattice matching with Mg at the inter-

face with the lattice misfit of 7.9% when it nucleates Mg solid on its faceted  $\{1\ 1\ 1\}$  or  $\{1\ 0\ 0\}$  surfaces [28,70]. With intensive melt shearing prior to solidification, the native MgO particles in the melt are well dispersed and the number density of the particles can be as high as  $\sim 10^{17}/\text{m}^3$  [81], 3 order of magnitude higher than  $\sim 10^{14}/\text{m}^3$  of  $\text{TiB}_2$  when 0.1% Al-5Ti-1B grain refiner is introduced in Al melt [56]. Given the current situation in the Mg industry where no commercial grain refiner is available, except Zr, which is only for Al-free Mg alloys, harnessing the native oxides in Mg alloy melts to achieve grain refinement is of great significance [74,80].

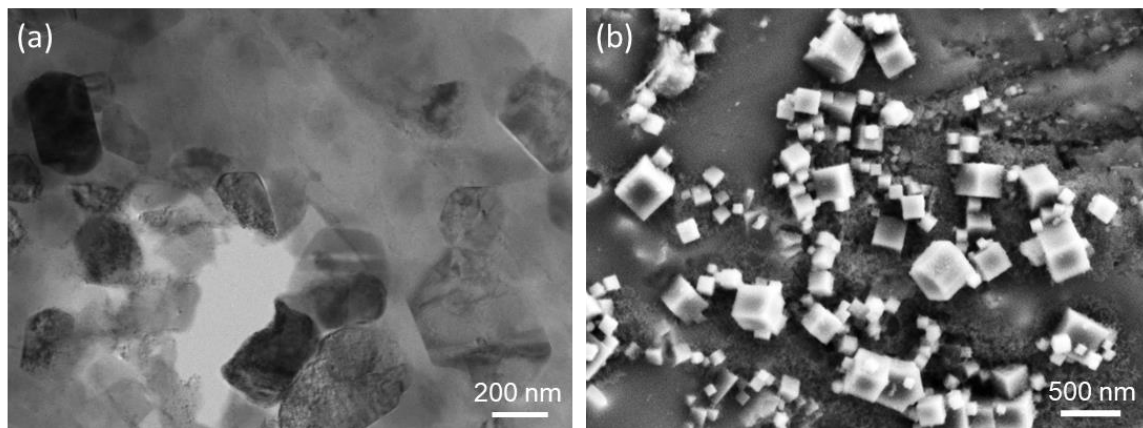


**Figure 24.** Faceted behaviour of the native MgO particles in Mg alloy melt [40,70,71]. TEM and SEM images showing (a)  $\{1\ 1\ 1\}$  faceted octahedral and (b)  $\{1\ 0\ 0\}$  faceted cubic MgO particles in Mg-9Al-1Zn (AZ91) alloy.

#### 4.3. Mg/MgO Interface

Among the two types of morphology, i.e.,  $\{1\ 1\ 1\}\text{MgO}$  and  $\{1\ 0\ 0\}\text{MgO}$  faceted, the  $\{1\ 1\ 1\}\text{MgO}$  particles are dominant in terms of particle numbers [40,70]. Well-defined ORs has been observed experimentally by high resolution TEM examinations of multiple MgO particles. As shown in Figure 25, two ORs between the two types, MgO and Mg, have been identified as [40,70,71]:

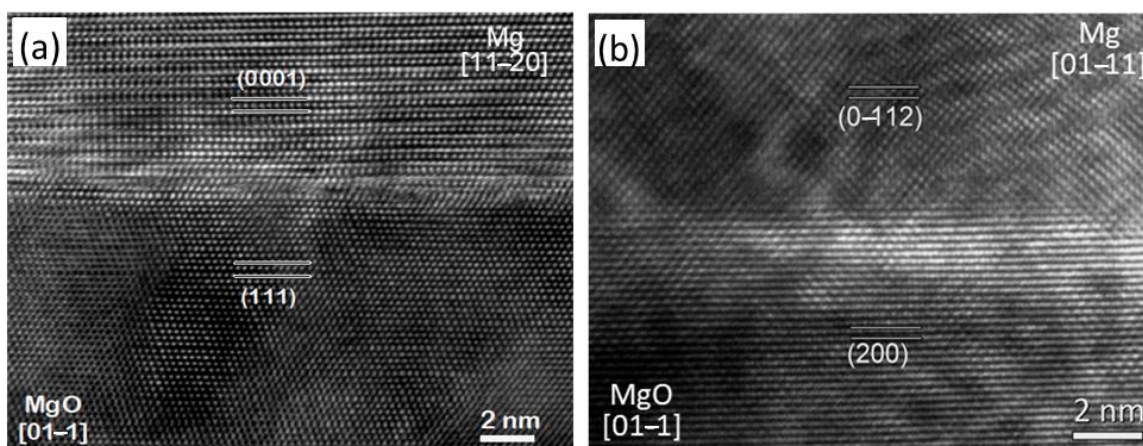


**Figure 25.** Evidence of heterogeneous nucleation of Mg on MgO particle substrate [40,71]. HR-TEM images viewed in (a)  $[1\ 1\ \bar{2}\ 0]\text{Mg} // [0\ 1\ \bar{1}]\text{MgO}$ , and (b)  $[0\ 1\ \bar{1}\ 1]\text{Mg} // [0\ 1\ \bar{1}]\text{MgO}$  direction, respectively, showing the well defined orientation relationships (ORs) between (a) Mg and  $\{1\ 1\ 1\}\text{Mg}$ , and (b) Mg and  $\{1\ 0\ 0\}\text{MgO}$ .

$$\text{OR3 : } (1\ 1\ 1)\ [0\ \bar{1}\ 1]\text{MgO} // (0\ 0\ 0\ 1)\ [1\ 1\ \bar{2}\ 0]\text{Mg},$$

$$\text{OR4 : } (2\ 0\ 0)\ [0\ 1\ \bar{1}]\text{MgO} // (0\ \bar{1}\ 1\ 2)\ [0\ 1\ \bar{1}\ 1]\text{Mg}.$$

This is the direct evidence that solid Mg does nucleate heterogeneously on both  $\{1\ 1\ 1\}$  and  $\{1\ 0\ 0\}$  MgO particles.

Ab initio molecular dynamics (AIMD) simulation has been carried out to study the terminating surfaces of MgO and the ordering of atoms in the local region of melt adjacent to the L-Mg/MgO interface at a temperature above the liquidus, i.e., prenucleation [82]. Figure 26a,b shows the snapshots of in-plane view of the newly formed terminating Mg layer on the  $\{1\ 1\ 1\}$ MgO surface and the corresponding sideview of the Mg/ $\{1\ 1\ 1\}$ MgO interface, respectively, after the thermodynamically equilibrium state was reached during the simulation at 1000 K. The new terminating layer was found to contain vacancies (marked by the crosses in Figure 26b), introducing roughness on the atomic scale to the  $\{1\ 1\ 1\}$  MgO surface and, thus, greatly weakening the atomic layering in the melt adjacent to the L/S interface, as shown in Figure 26b.

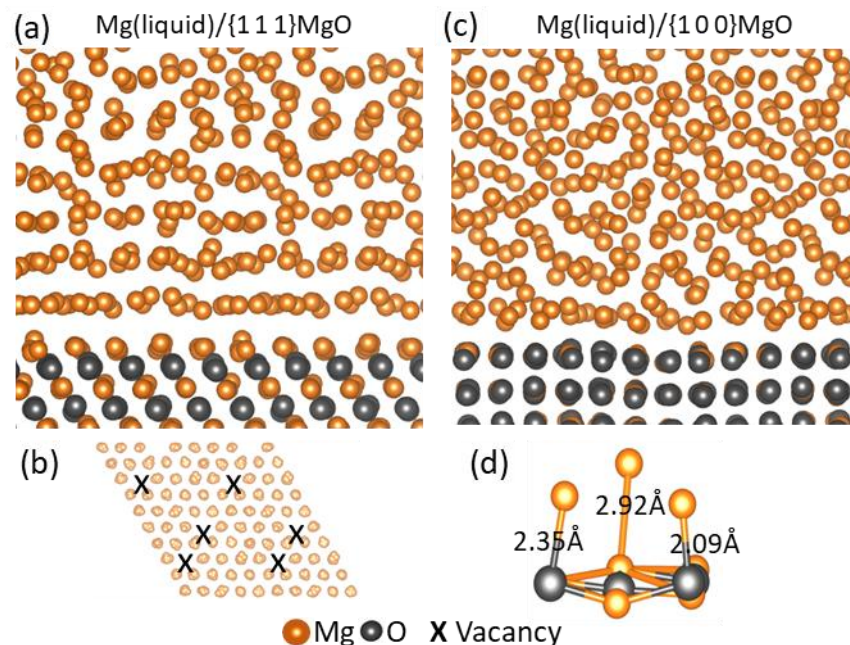


**Figure 26.** Ab initio molecular dynamics (AIMD) simulation of Mg/MgO interface [82]. (a) Mg(l)/MgO $\{1\ 1\ 1\}$  and (c) Mg(l)/MgO $\{0\ 0\ 1\}$  interfaces showing atomically rough; (b) the first liquid Mg layer induced by the usually O-terminated MgO $\{1\ 1\ 1\}$  substrate, containing vacancies as marked by the “x”; and (d) the first liquid Mg layer induced by the MgO $\{0\ 0\ 1\}$  substrate, showing atomically rough due to the varying bond lengths between liquid Mg atoms and the O and Mg ions on the MgO $\{0\ 0\ 1\}$  surface.

Figure 26c,d shows chemical bonding of liquid Mg atoms to the adjacent O and Mg ions in the  $\{0\ 0\ 1\}$ MgO substrate and the snapshot of the side view of the Mg/ $\{1\ 0\ 0\}$ MgO interface at the equilibrium state in the simulation. The bond length between Mg<sup>2+</sup> ion on the  $\{1\ 0\ 0\}$ MgO surface and Mg atom in the melt was 2.92 Å, 0.8 Å longer than that between O<sup>2-</sup> ion and Mg atom in the melt (Figure 26d), and the surface of  $\{1\ 0\ 0\}$  MgO was atomically rough [82]. Consequently, the ability of  $\{1\ 0\ 0\}$  MgO to template ordering of the atoms in the melt was strongly reduced, i.e., a decreased prenucleation [82].

#### 4.4. Y Segregation at Mg/MgO $\{1\ 1\ 1\}$ Interface

Yttrium (Y) is one of the rare earth elements which enables high performance of some advanced Mg- alloys, such as the WE series alloys. Y present in Mg alloy melts has been readily found to segregate at the Mg/MgO interface. Figure 27 shows the experimental evidence of Y segregation in Mg-0.5Y melt at the interface between  $\{1\ 1\ 1\}$  faceted MgO and Mg, where the peaks of yttrium L edge losses clearly appear in the STEM/EELS spectrum in Figure 26a (curve 2 in orange), acquired from the local area at Mg/MgO interface. The



local STEM HAADF image (Figure 27b) from  $[0\ 1\ 1]_{\text{MgO}}$  direction and corresponding EELS elemental map of yttrium (Figure 27c) verify the Y segregation at the interface [28].

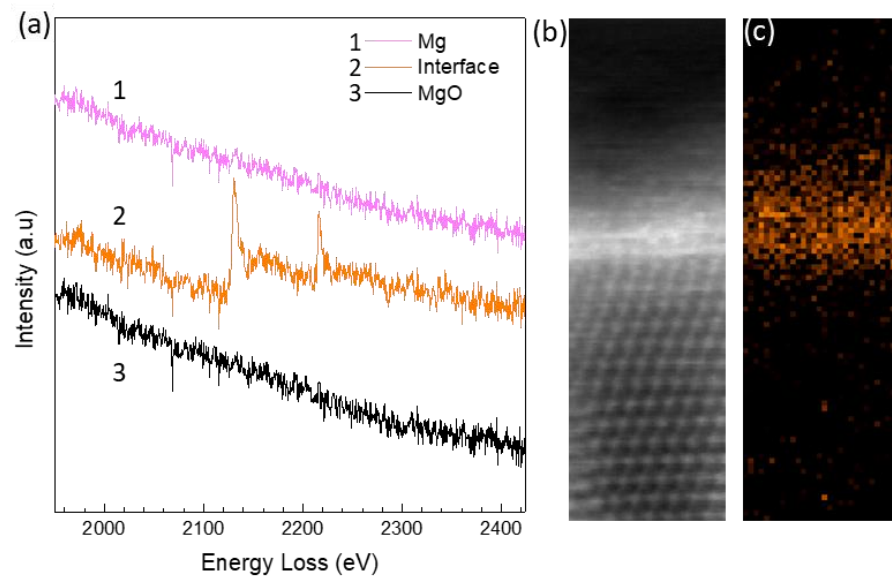
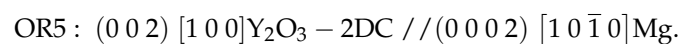


**Figure 27.** Yttrium segregation at Mg/ $(1\ 1\ 1)_{\text{MgO}}$  interface [28]. (a) STEM/EELS spectra acquired from areas of Mg (curve 1), MgO/Mg interface (curve 2) and MgO (curve 3) where yttrium edge loss is clearly seen from curve 2; (b) STEM HAADF image along  $[0\ 1\ 1]_{\text{MgO}}$  direction during EELS acquisition; and (c) corresponding EELS elemental map of yttrium, showing segregation of yttrium at the interface.

High resolution STEM HAADF images in Figure 28a,b show the Mg/ $(1\ 1\ 1)_{\text{MgO}}$  interface observed in  $[2\ \bar{1}\ 1]_{\text{MgO}}$  and  $[0\ 1\ 1]_{\text{MgO}}$  directions, respectively. There are two interfacial atomic layers in which the atomic columns exhibit a higher brightness than (Mg, O) columns of MgO (O columns are invisible) in the HAADF images, verifying the presence of Y atoms in the two layers. Extensive STEM/EELS revealed that O atoms were also involved in the segregation region and an O layer was located between the two Y-containing layers [28,29]. In terms of both the structure and chemistry, it was found that the 3 segregation layers, i.e., two Y layers and one O layer in between, resembled the three  $\{1\ 0\ 0\}$  layers of an fcc  $\text{Y}_2\text{O}_3$  unit cell, although the measured spacing  $2.73\ \text{\AA}$  between the two Y layers was slightly larger than  $2.632\ \text{\AA}$  [83], the d-spacing of  $\{2\ 0\ 0\}_{\text{Y}_2\text{O}_3}$  planes indicating that interfacial segregation of Y atoms from alloy melt led to the formation of  $\text{Y}_2\text{O}_3$  2DC. Figure 28c,d illustrate schematically the atomic configuration of the segregated Y atoms viewed from  $[2\ \bar{1}\ 1]_{\text{MgO}}$  direction and 3D construction of the  $\text{Y}_2\text{O}_3$  2-dimensional compound (2DC) at the interface.

With the formation of  $\text{Y}_2\text{O}_3$  2DC at the Mg/ $(1\ 1\ 1)_{\text{MgO}}$  interface, Mg nucleates on the  $\text{Y}_2\text{O}_3$  2DC, instead of on the  $(1\ 1\ 1)_{\text{MgO}}$  surface. The lattice misfit at the interface is, therefore, calculated as 1.71%, much smaller than the initial value of 7.9% between Mg and MgO, according to the OR5 below [28]:



The much-reduced lattice misfit between  $\text{Y}_2\text{O}_3$  2DC and Mg indicates an increased nucleation potency for MgO substrate with the Y segregation. In addition, the heat of mixing between Y and Mg was reported as  $\sim 6\ \text{kJ/mol}$  [84], suggesting a strong affinity between Y and Mg atoms. A promotion of prenucleation is, therefore, expected in the melt close to the Mg melt/ $\text{Y}_2\text{O}_3$ -2DC interface due to the potential chemical reaction between Mg and Y atoms, subsequently promoting nucleation potency.

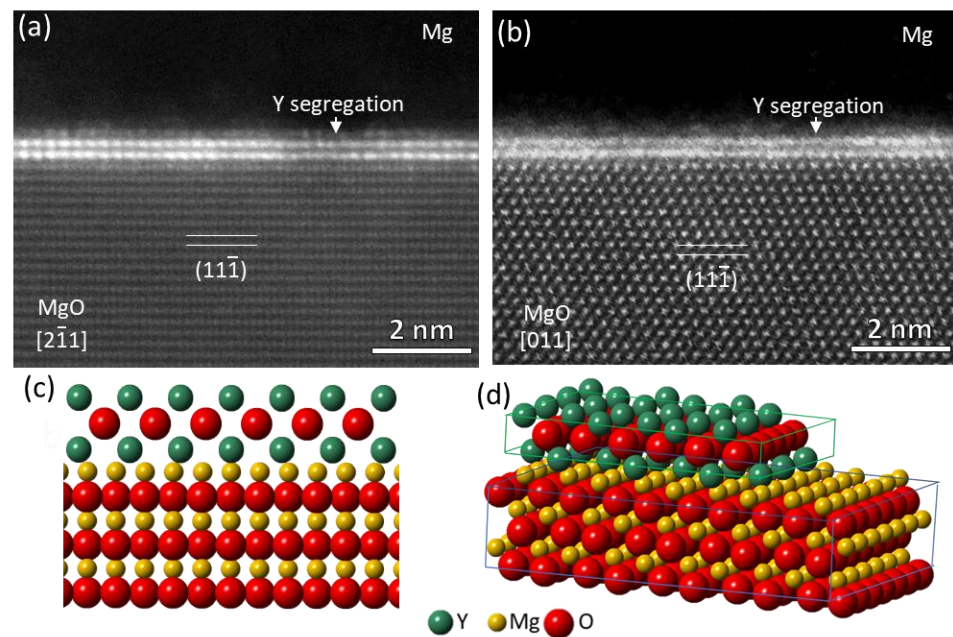


**Figure 28.** Nature of Y segregation layer at Mg/(1 1 1)MgO interface [28]. (a,b) High resolution STEM HAADF images showing interface between Mg and (1 1 1)MgO particle along (a)  $[2 \bar{1} 1]_{\text{MgO}}$  and (b)  $[0 1 1]_{\text{MgO}}$  direction respectively, where two Y-containing atomic layers with a brighter contrast are visible; and (c,d) schematics showing (c) segregated Y atoms viewed from  $[2 \bar{1} 1]_{\text{MgO}}$  direction and (d) 3D construction of  $\text{Y}_2\text{O}_3$  2DC segregation layer.

#### 4.5. Y Segregation at Mg/MgO{1 0 0} Interface

Y segregation is also observed on the surface of {1 0 0} surface of cubic MgO particles in Mg-0.5Y melt. However, the behaviour of Y segregation on the {1 0 0} MgO surface is considerably different from that on the {1 1 1} MgO surface [28]. From  $[0 0 1]_{\text{MgO}}$  and  $[0 1 1]_{\text{MgO}}$  directions, respectively, the STEM HAADF images in Figure 29 show that the atomic columns in an atomic monolayer at the Mg/(1 0 0)MgO interface have a high bright contrast, indicating that Y atoms are in the atomic layer. When viewed in  $[0 0 1]_{\text{MgO}}$ , Y-containing atomic columns are seen in every other (Mg, O) column of the top (1 0 0)MgO plane, resulting in the periodic brightness pattern, i.e., the brighter column appearing on every other column when viewed from  $[0 0 1]_{\text{MgO}}$  direction, as shown in Figure 29a. The brightness pattern of the monolayer disappears when viewed from the  $[0 1 1]_{\text{MgO}}$  direction, as shown in Figure 29b. This indicates that Y atoms are present only in the Mg columns of the top (1 0 0)MgO layer.

It was also noted that the Y-containing atomic columns of the monolayer were elongated vertically when viewed from both  $[0 0 1]_{\text{MgO}}$  and  $[0 1 1]_{\text{MgO}}$  directions, with the protrusion being experimentally measured as 0.62 Å [28]. Further analysis showed that this was because only part of the Mg atoms in the columns of the top (1 0 0) MgO layer were substituted by Y atoms, with the Y atoms being protruded relative to the remaining Mg alloys in the column [28]. Figure 29c,d are schematics, showing the atomic configuration of the segregated Y atoms viewed from the  $[0 0 1]_{\text{MgO}}$  direction and 3D construction of the monolayer on the (1 0 0) surface of MgO.

The Y-containing atomic monolayer on the {1 0 0} facets of the cubic MgO was coherent with the top {1 0 0}Mg plane, and, therefore, the lattice misfit between the newly formed monolayer and Mg remained the same as before. However, an atomic roughness was introduced to the monolayer due to the vertical protrusion by 0.62 Å of the Y atoms, which reduced the nucleation potency of the {1 0 0} cubic MgO and, thus, impeded prenucleation [9,82].

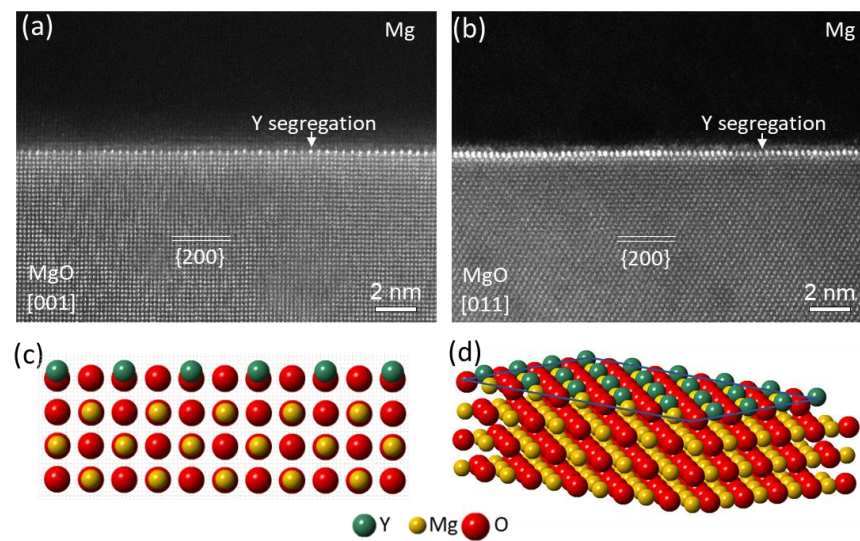


**Figure 29.** Nature of Y segregation layer at Mg/(1 0 0)MgO interface [28]. (a,b) High-resolution STEM HAADF images of (1 0 0)Mg/MgO interface viewed along (a) [0 0 1]MgO and (b) [0 1 1]MgO direction respectively, showing a bright atomic monolayer at the interface; and (c,d) schematics showing (c) segregated Y atoms viewed from [0 0 1] MgO direction and (d) 3D construction of the Y-containing monolayer on (1 0 0) surface of MgO.

#### 4.6. Segregation of Ca and Sn at Mg/MgO Interface

As one of the essential alloying elements in advanced high-performance Mg alloys, Ca is found to segregate readily at the Mg/MgO interface of native MgO particles. Figure 30 shows the evidence of Ca segregation, where a layer about 1 nm thick is seen at the Mg/(1 1 1)MgO interface, appearing in a relatively lower contrast compared with MgO in the HAADF image in Figure 30a. STEM/EELS acquired from different positions across the interface in Figure 30b,c indicate that the chemistry of the segregation layer differs from that of MgO or Mg matrix. Ca segregation at the Mg/MgO interface is associated with N which comes from the protection atmosphere during casting process. Detailed analyses showed [29,77] that the Ca segregation layer at Mg/MgO particles had a crystal structure resembling that of the bulk MgO crystal, with Ca and N atoms selectively substituting some of the Mg and O atoms on the MgO surface, respectively. The co-segregation of Ca and N results in a surface roughness and in-plane disordering, which, in turn, makes the pre-nucleation difficult, reducing nucleation potency of the MgO modified by the co-segregation of Ca and N.

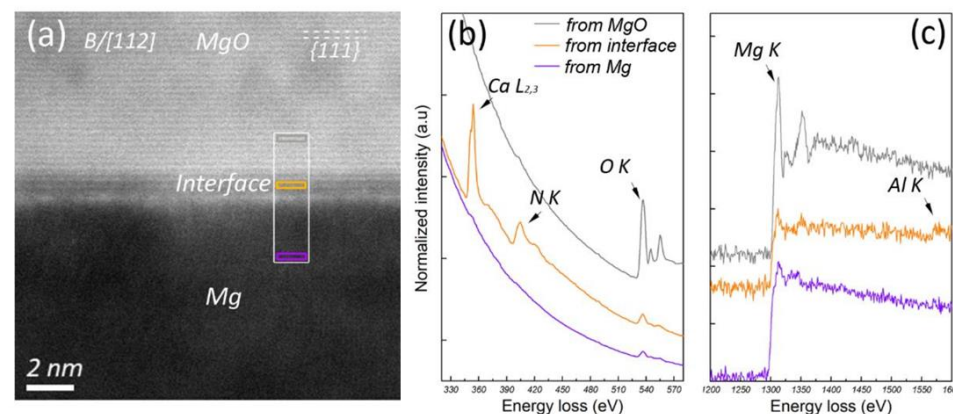


**Figure 30.** Ca segregation at Mg/(1 1 1)MgO interface [29,77]. (a) STEM-HAADF image of interface between Mg and MgO, showing a segregation layer at the interface; (b,c) EELS spectra acquired from different areas across the interface as indicated in the HAADF image.

Figure 31 gives evidence of Sn segregation at the Mg/(1 0 0)MgO interface. The HAADF images in Figure 31a,b show that there is a layer with a brighter contrast at the interface, apparently indicating an enrichment in Sn at the interface. The EELS in Figure 31c,d confirms the Sn segregation. It is shown that the segregated Sn atoms selectively substitute some of the Mg atoms in MgO without changing the lattice structure [29]. Detailed chemical and structural revealed that, with Sn segregation at the Mg/MgO interface, a roughness on the atomic scale was introduced and, thus, the ability for Mg to pre-nucleate on the MgO particles decreased [29].

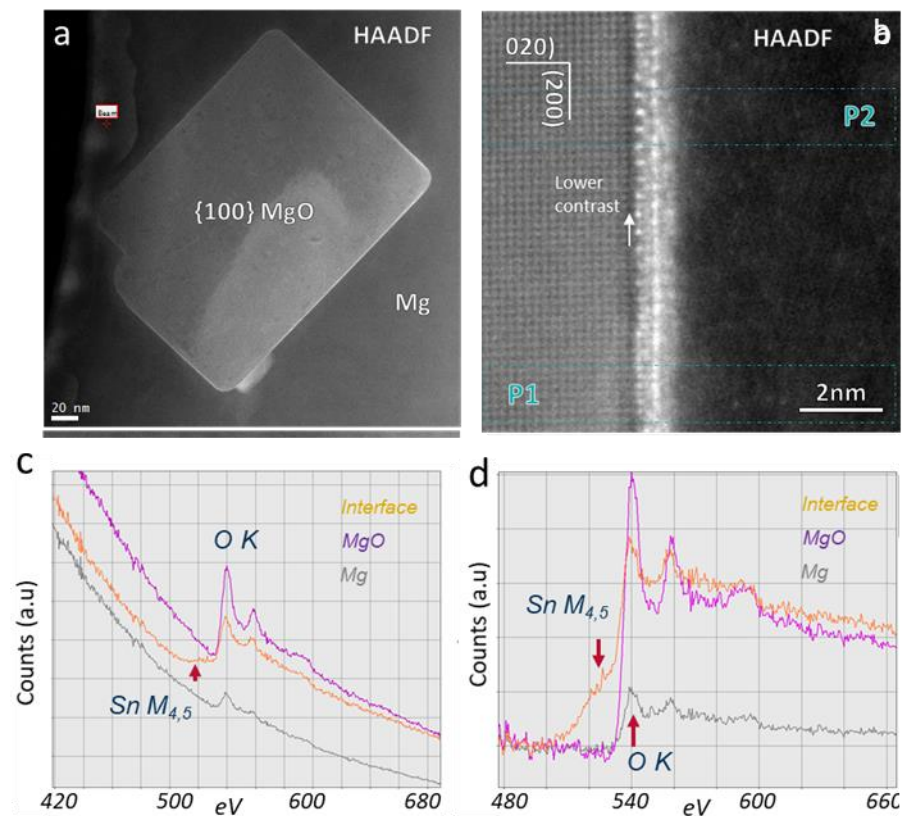


**Figure 31.** Sn segregation at Mg/(1 0 0)Mg interface [29]. (a,b) STEM HAADF images showing (a) general view of a {1 0 0} cubic MgO and (b) the Mg/MgO interface viewed in [0 0 1]MgO direction; and (c,d) the EELS spectra without and with background subtraction suggesting that Sn exists at the interface (indicated by the arrows).

## 5. Segregation at Al/ $\gamma$ -Al<sub>2</sub>O<sub>3</sub> Interface

### 5.1. Nature of $\gamma$ -Al<sub>2</sub>O<sub>3</sub>

Liquid Al oxidizes readily at the surface when it is exposed to an atmosphere containing oxygen and/or water moisture, producing two major types of alumina,  $\gamma$ -Al<sub>2</sub>O<sub>3</sub> and  $\alpha$ -Al<sub>2</sub>O<sub>3</sub>, with different crystal structures. The alumina is subjected to transformation from  $\gamma$ -Al<sub>2</sub>O<sub>3</sub> to  $\alpha$ -Al<sub>2</sub>O<sub>3</sub> with increasing time and temperature. The formation of  $\alpha$ -Al<sub>2</sub>O<sub>3</sub> was reported to occur at temperatures higher than 850 °C in Al-alloy melts [85]. Over the temperature range involved for cast processing of Al-alloys, typically lower than 750–800 °C, the native alumina formed in the melts are  $\gamma$ -Al<sub>2</sub>O<sub>3</sub> [75,86–89]. However, Mg addition to Al alloys results in change of the oxide from Al<sub>2</sub>O<sub>3</sub> to MgAl<sub>2</sub>O<sub>4</sub> spinel or MgO, depending on Mg concentration [75,86,89]. The alumina in commercially pure Al (CP-Al) at 750 °C are usually in the form of films (Figure 32a) containing enormous individual  $\gamma$ -Al<sub>2</sub>O<sub>3</sub> particles (Figure 32b). Typically,  $\gamma$ -Al<sub>2</sub>O<sub>3</sub> particles in CP-Al melt display platelet-like morphology, about 50 nm thick and 200–300 nm long on average (Figure 33a). {1 1 1} crystal planes are the terminating surfaces of the faceted alumina platelets, and twins along the {1 1 1} planes

are also frequently observed inside them (Figure 33b). For convenience,  $\gamma\text{-Al}_2\text{O}_3$  with a  $\{1\ 1\ 1\}$  faceted morphology is denoted as  $\gamma\text{-Al}_2\text{O}_3\{1\ 1\ 1\}$ .

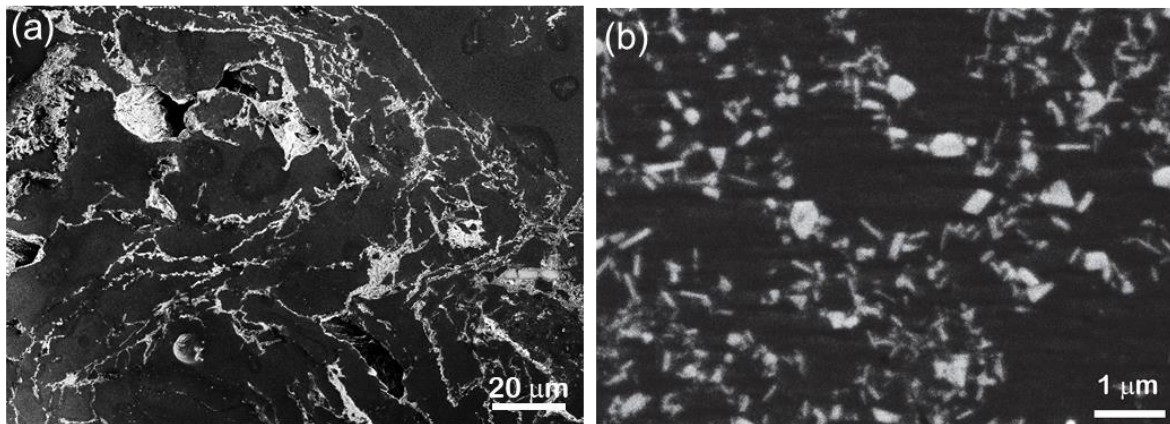


**Figure 32.** Morphology of native  $\gamma\text{-Al}_2\text{O}_3$  films/particles in CP-Al [75,86]. SEM micrographs showing the general view of (a)  $\gamma\text{-Al}_2\text{O}_3$  films at low magnification and (b) the discrete  $\gamma\text{-Al}_2\text{O}_3$  particles collected from commercial purity Al (CP-Al) at 750 °C by melt filtration.

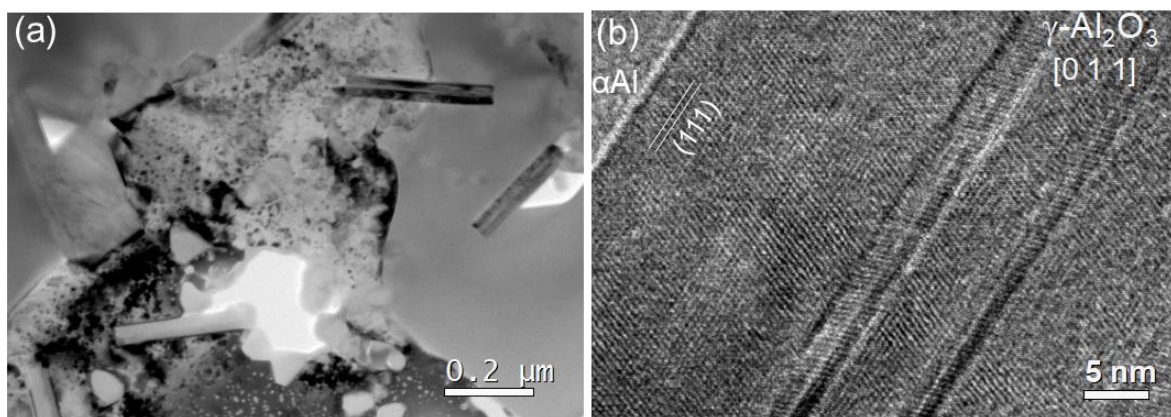


**Figure 33.** Faceted behavior of the native  $\gamma\text{-Al}_2\text{O}_3$  particles in CP-Al melt [75,86]. TEM micrograph showing (a) the typical morphology of the faceted  $\gamma\text{-Al}_2\text{O}_3$  particles in commercial purity Al (CP-Al) melt, which display a platelet-like morphology about 50 nm thick and 200–300 nm long on an average; and (b) high resolution TEM micrograph showing the  $\gamma\text{-Al}_2\text{O}_3$  particle is faceted and twinned along its  $\{1\ 1\ 1\}$  planes.

### 5.2. Y Segregation at Al/ $\gamma\text{-Al}_2\text{O}_3$ Interface

$\text{Al}_2\text{O}_3$  particles were collected from Al-0.075Y alloy melt and segregation of Y at the interface between Al and  $\{1\ 1\ 1\}$  terminating surface of  $\gamma\text{-Al}_2\text{O}_3$  was investigated. The experimental results revealed the evidence of Y segregation at the Al/ $\gamma\text{-Al}_2\text{O}_3$  interface, which was consistently observed by high resolution STEM-HAADF/ADF images, STEM/EDS mapping and STEM/EELS analysis, etc. Figure 34a is a Z-contrast STEM-HAADF image of Al/ $\gamma\text{-Al}_2\text{O}_3$  interface, where a monolayer with a brighter contrast than the  $\gamma\text{-Al}_2\text{O}_3$  is observed. The yttrium atom was much heavier than Al ( $Z_{\text{Y}} = 39$  vs.  $Z_{\text{Al}} = 13$ ), so the brighter contrast in the HAADF image suggests Y enrichment in the monolayer at the interface. The arrangement of Y-rich atomic columns in the monolayer was identical to the high-density Al columns in the  $\gamma\text{-Al}_2\text{O}_3$  crystal, having an interatomic spacing of  $1/2 \langle 011 \rangle_{\gamma\text{-Al}_2\text{O}_3}$ . The Y segregation layer was found to cover the whole Al/ $\gamma\text{-Al}_2\text{O}_3$  interface, confirmed by the STEM/EDS mapping in Figure 34b–d.

Ab initio molecular dynamics (AIMD) simulation was performed to clarify the above experimental evidence of Y interfacial segregation and to reveal the effect of segregation

on the atomic ordering of liquid atoms close to the L-Al/ $\gamma$ -Al<sub>2</sub>O<sub>3</sub>{1 1 1} interfaces. As shown in Figure 35a,b, Y atoms (large dark green spheres) in Al melt tend to segregate at the L-Al/ $\gamma$ -Al<sub>2</sub>O<sub>3</sub>{1 1 1} interface, due to their lower electronegativity values than Al and higher stability of yttria than that of alumina. Both structurally and chemically, Y segregation results in the formation of approximately Al<sub>2</sub>Y two-dimensional compound (2DC) and the reconstruction of the metal layers adjacent to the surface of the  $\gamma$ -Al<sub>2</sub>O<sub>3</sub>{1 1 1} substrate, in agreement with the HR-STEM results. It was also seen from the atomic density profiles in Figure 35c,d that the segregated Y atoms protruded into the alloy melt with respect to the Al atoms, and this splitting of the terminating layer would introduce an atomic roughness to the {1 1 1} surface of the  $\gamma$ -Al<sub>2</sub>O<sub>3</sub>. As a consequence, the potency of the  $\gamma$ -Al<sub>2</sub>O<sub>3</sub> substrate for nucleation of Al was weakened. Figure 35e,f show the top view of the in-plane atomic arrangement of the Y segregation layer at the Al/ $\gamma$ -Al<sub>2</sub>O<sub>3</sub> interface, showing the atomic arrangement of the Al<sub>2</sub>Y 2DC.

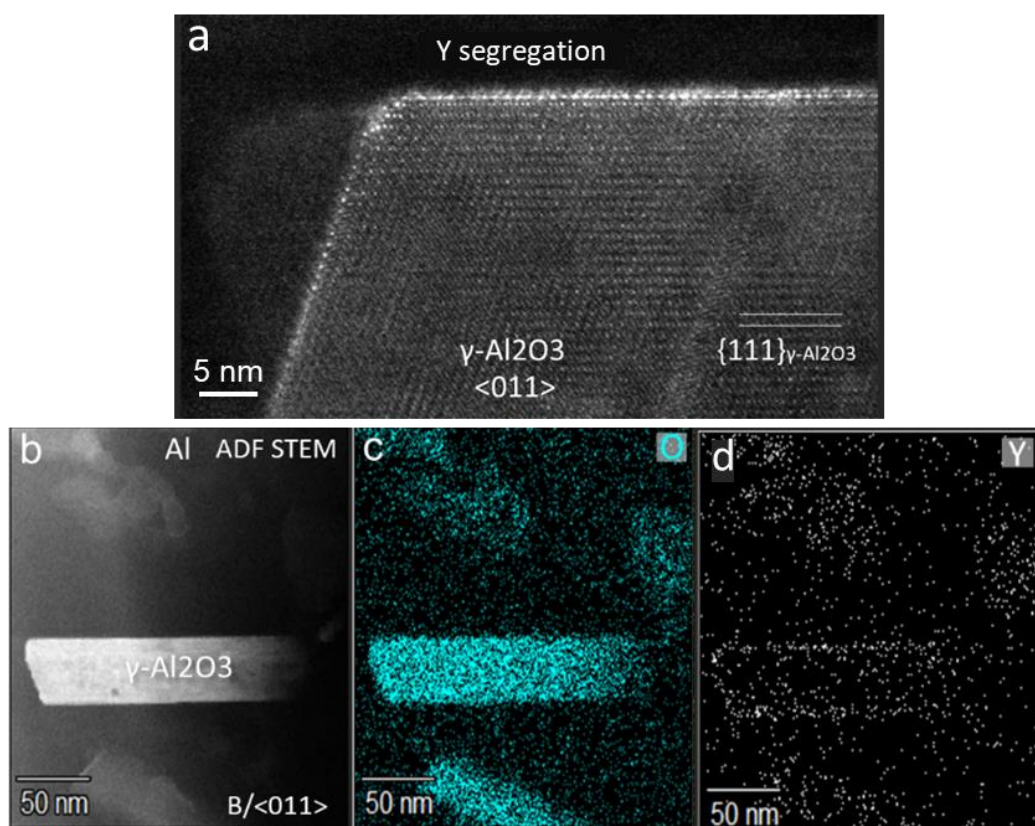


**Figure 34.** Y segregation at Al/ $\gamma$ -Al<sub>2</sub>O<sub>3</sub> interface. (a) STEM-HAADF image of Al/ $\gamma$ -Al<sub>2</sub>O<sub>3</sub> interface for a  $\gamma$ -Al<sub>2</sub>O<sub>3</sub> particle in Al-0.075Y alloy; (b) STEM ADF image; and EDS elemental mapping of (c) O and (d) Y, showing Y enrichment at the interface.

### 5.3. La Segregation at Al/ $\gamma$ -Al<sub>2</sub>O<sub>3</sub> Interface

La segregation was readily observed at Al/ $\gamma$ -Al<sub>2</sub>O<sub>3</sub> interfaces during the examination of multiple numbers of  $\gamma$ -Al<sub>2</sub>O<sub>3</sub> particles in Al-0.075La and Al-0.75La alloys [88]. Figure 36 shows a STEM-HAADF/ADF image and STEM/EDS maps covering a  $\gamma$ -Al<sub>2</sub>O<sub>3</sub> particle from Al-0.75La alloy melt, where a brighter monolayer at the interface is clearly visible, with the brighter atomic columns in the monolayer arranged in an interatomic spacing of  $\frac{1}{2} < 0 1 1 >_{\gamma\text{-Al}_2\text{O}_3}$ . The existence of La in the bright atomic columns of the monolayer was further confirmed by the EDS map of La in Figure 36d, where La segregation was seen to continuously cover the Al/ $\gamma$ -Al<sub>2</sub>O<sub>3</sub> interface.

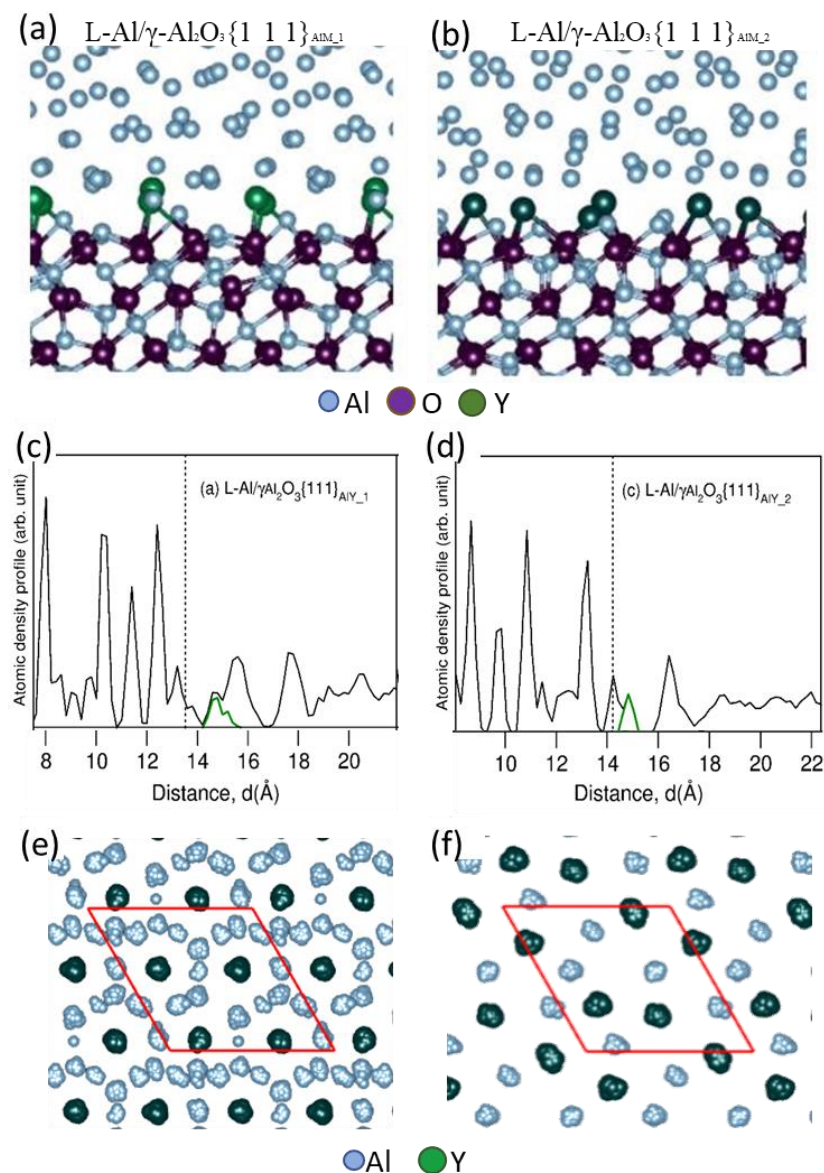


**Figure 35.** Ab initio molecular dynamics (AIMD) simulation of Y segregation at L-Al/ $\gamma$ -Al<sub>2</sub>O<sub>3</sub> interface. (a,b) Snapshots of Y segregation at (a) L-Al/ $\gamma$ -Al<sub>2</sub>O<sub>3</sub>{1 1 1}<sub>AIM\_1</sub> and (b) L-Al/ $\gamma$ -Al<sub>2</sub>O<sub>3</sub>{1 1 1}<sub>AIM\_2</sub> interfaces at equilibrium at 1000 K; (c,d) atomic density profiles  $\rho(z)$  of Y segregated at the L-Al/ $\gamma$ -Al<sub>2</sub>O<sub>3</sub>{1 1 1}<sub>AIM</sub> interfaces where the black curve represents  $\rho(z)$  for all atoms, while the dark-green curve is for Y; and (e,f) top view of in-plane atomic arrangement of the Y segregation layer at the L-Al/ $\gamma$ -Al<sub>2</sub>O<sub>3</sub>{1 1 1}<sub>AIM</sub> interfaces. The blue spheres represent Al atoms, dark-brown O, and dark-green Y.

AIMD simulation of the L-Al/ $\gamma$ -Al<sub>2</sub>O<sub>3</sub> interface where La segregated showed similar results to that of the interface with Y segregation [88]. As shown in Figure 37, La atoms (light-green spheres) were found to segregate at the interface, with the structure and chemistry of the La-containing layer being similar to Al<sub>2</sub>La 2DC. In addition, the La atoms with a much larger atomic radius than Al atoms were seen to protrude into the alloy melt, as shown in Figure 37a,b. The protrusion of La atoms is clearly seen in the atomic density profiles in Figure 37c,d. Figure 37e,f show the top view of the in-plane atomic arrangement of the La segregation layer at the Al/ $\gamma$ -Al<sub>2</sub>O<sub>3</sub> interface, indicating the formation of Al<sub>2</sub>Y 2DC. Due to the protrusion of La atoms in the Al<sub>2</sub>La 2DC layer at the interface, the  $\gamma$ -Al<sub>2</sub>O<sub>3</sub> surface was atomically rough. The simulation revealed that, due to the atomic roughness

of the  $\text{Al}_2\text{O}_3$  surface, the prenucleation at the  $\text{L-Al}/\gamma\text{-Al}_2\text{O}_3\{1\ 1\ 1\}$  interface was weakened to a similar level by the interfacial segregation of Y and La atoms.

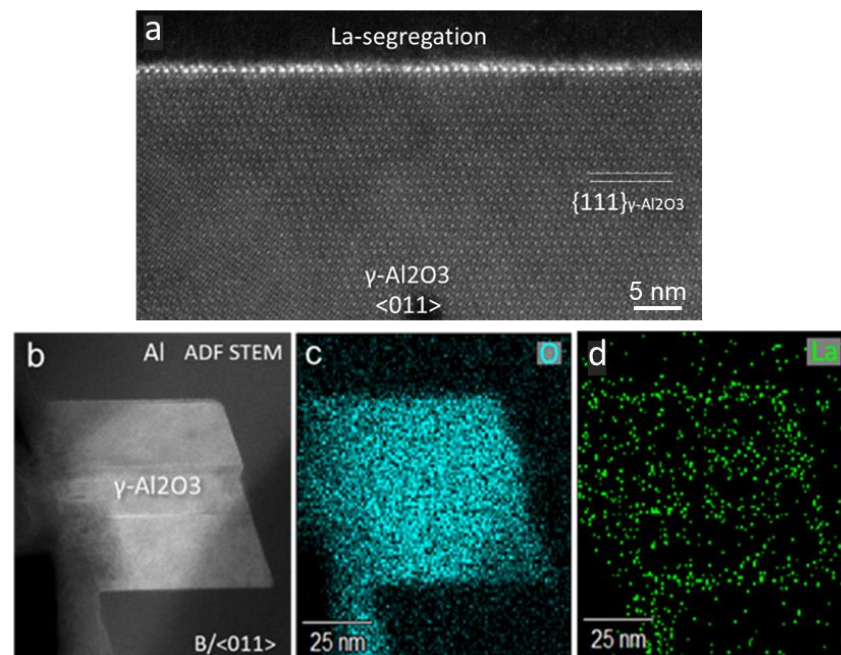


**Figure 36.** La segregation at  $\text{Al}/\gamma\text{-Al}_2\text{O}_3$  interface [88]. (a) STEM Z-contrast HAADF image of  $\text{Al}/\gamma\text{-Al}_2\text{O}_3$  interface for a  $\gamma\text{-Al}_2\text{O}_3$  particle in  $\text{Al-0.75La}$  alloy; (b) STEM ADF image; and (c,d) EDS elemental mapping of (c) O, (d) La, showing La enrichment at the interface.

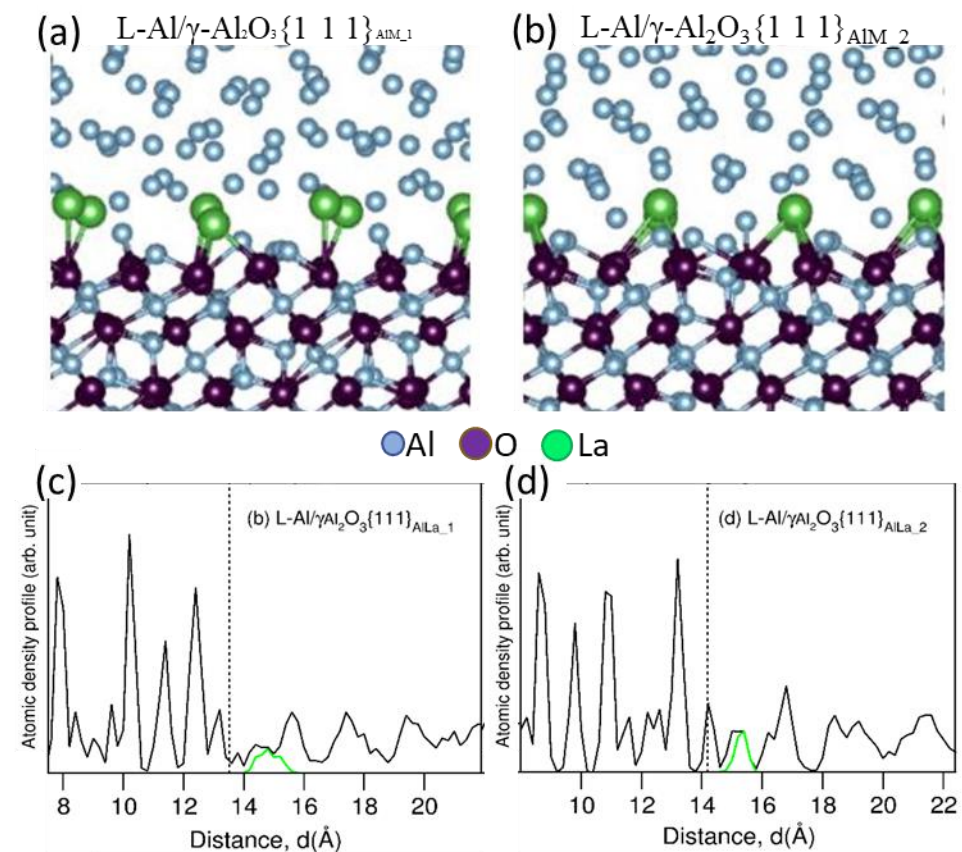


**Figure 37.** Cont.



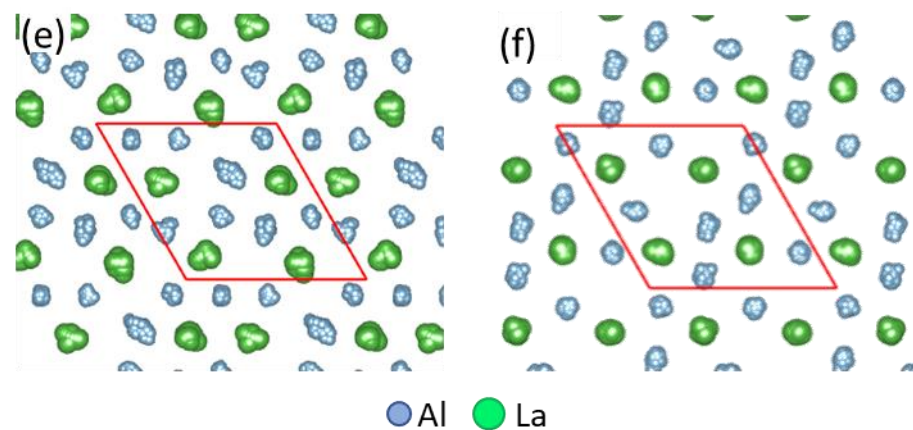


**Figure 37.** Ab initio molecular dynamics (AIMD) simulation of La segregation at L-Al/ $\gamma$ -Al<sub>2</sub>O<sub>3</sub> interface [88]. (a,b) Snapshots of La segregation at (a) L-Al/ $\gamma$ -Al<sub>2</sub>O<sub>3</sub>{1 1 1}<sub>AIM\_1</sub> and (b) L-Al/ $\gamma$ -Al<sub>2</sub>O<sub>3</sub>{1 1 1}<sub>AIM\_2</sub> interfaces at equilibrium at 1000 K; (c,d) atomic density profiles  $\rho(z)$  of La segregated at the L-Al/ $\gamma$ -Al<sub>2</sub>O<sub>3</sub>{1 1 1}<sub>AIM</sub> interfaces where the black curve represents  $\rho(z)$  for all atoms, while the light-green curve is for La; and (e,f) top view of in-plane atomic arrangement of the La segregation layer at the L-Al/ $\gamma$ -Al<sub>2</sub>O<sub>3</sub>{1 1 1}<sub>AIM</sub> interfaces. The blue spheres represent Al atoms, dark-brown O, and light-green La.

## 6. General Discussions

### 6.1. Manipulating Nucleation Potency of Substrate

Involving both heterogeneous nucleation and grain initiation processes, grain refinement is usually achieved by addition of grain refiners, i.e., chemical inoculation. During solidification of an alloy, heterogeneous nucleation is the process of creating a new solid phase on a nucleation substrate through structural templating, and, then, the new solid phase grows into the alloy melt. With a certain undercooling of the melt, nucleation occurs on all the substrate particles of the same kind which have the same nucleation potency, regardless of the substrate size. According to the epitaxial nucleation model [8], the critical undercooling  $\Delta T_n$  required for nucleation to be triggered on a given type of substrate is determined by the nucleation potency of the substrate, and the nucleation process proceeds in a layer-by-layer fashion through a structural templating mechanism. As an indication of nucleation potency, nucleation undercooling  $\Delta T_n$  is dependent on lattice misfit at the interface between the new solid phase and the substrate [8,63], atomic level surface roughness of the substrate [9], and chemical interaction between the substrate and the alloy melt [10].

With nucleation being triggered, whether the nucleated new solid phase can grow freely or not, i.e., grain initiation into a grain eventually after solidification is determined by grain initiation undercooling  $\Delta T_{gi}$  according to the free growth model [56]. This model explains that, by overcoming the energy barrier for grain initiation after nucleation, a nucleated solid phase can freely grow only when its size is larger than a critical value to overcome the curvature constraint. Given a natural size distribution of substrate particles, the larger nucleated solid particles require smaller grain initiation undercooling  $\Delta T_{gi}$  and, thus, grow first, so that the grain initiation process proceeds in a progressive manner.

The traditional wisdom used in development of grain refinement is to search for the most potent solid particles to reduce nucleation undercooling  $\Delta T_n$ . For instance, Al-Ti-B based master alloys have been used as effective grain refiners for Al alloys for more than six decades in industry [1,2,90]. As demonstrated above, the high grain refining effectiveness of the Al-Ti-B master alloys is attributed to the formation of an Al<sub>3</sub>Ti 2DC layer on the TiB<sub>2</sub> particle surface [11], reducing the absolute lattice misfit at the Al/TiB<sub>2</sub> interface from 4.22% to 0.09% and, thus, leading to a substantial increase in nucleation potency with a very small  $\Delta T_n$  [91]. With improvements made over the last six decades, the commercial Al-Ti-B grain refiners are now very effective and the TiB<sub>2</sub> particles in the refiners are optimized in terms of their particle size and size distribution [92].

The same wisdom has been used in search for grain refiners for Mg-based alloys. Currently, Mg-Zr is the grain refiner commercially available for Al-free Mg alloys [6,7], with the solid Zr particles in the grain refiner acting as the effective nucleation substrates for Mg due to their high potency. Since Zr has the same hcp crystal structure, and very similar lattice parameters to that of Mg, it, thus, has a small lattice misfit of 0.67% with Mg. However, Mg-Zr refiner does not work for Al-bearing Mg alloys, due to its reaction with Al.

With potent nucleation substrates, such as TiB<sub>2</sub> with Al<sub>3</sub>Ti-2DC, on their surface Al alloys, or Zr for Mg alloys, heterogeneous nucleation occurs with a small nucleation undercooling  $\Delta T_n$  and grain initiation proceeds progressively, usually resulting in a grain size of a few hundreds of microns [92].

In contrast to the conventional wisdom, Fan et al. [80] have recently developed new approaches to achieve more significant grain refinement by introducing explosive grain initiation (EGI) as a new grain initiation mode. By increasing nucleation undercooling  $\Delta T_n$ , EGI has the potential to push grain refinement to a new level unachievable by conventional approaches. This has been demonstrated in the experiments of Mg grain refinement by native MgO particles. For instance, the grain size of Mg-9Al alloy has been refined as small as 67  $\mu\text{m}$  under a cooling rate of 3.5 K/s, and even down to a few micrometers under high pressure die-casting conditions ( $\sim 1000$  K/s cooling rate) by partial realization of EGI [80]. Native MgO in a Mg alloy melt has a large lattice misfit with  $\alpha$ -Mg (7.9%) [70], a small particle size (50–200 nm) [40,70] and a large number density ( $\sim 10^{17}\text{m}^{-3}$  after melt shearing) [81]. This makes MgO impotent for heterogeneous nucleation but effective to promote EGI for more effective grain refinement.

From the viewpoint of alloy recycling, harnessing the native solid particles in alloy melts for grain refinement is preferable to the traditional chemical inoculation. In terms of the numbers of the particles which participate in nucleation and grain initiation, chemical inoculation is inefficient, since only a small fraction of the added nucleation particles (<1%) are effective for grain initiation [56]. This means that the majority of the added particles end up in the inter-dendritic regions of the solidified microstructure, leading to an adverse effect on the mechanical properties. In addition, accumulation of the inoculant particles causes severe contamination in the recycled alloys, making recycling increasingly difficult.

## 6.2. Engineering Liquid/Substrate Interface for Grain Refinement

Alloying elements or impurities are usually observed to segregate at various interfaces, such as liquid/substrate interface, grain boundaries and surfaces, resulting in significant effects to the properties of the interfaces or surfaces. Generally, equilibrium segregation at an interface describes distribution of solutes governed by minimization of total free energy of the systems. Theoretically, the Gibbs adsorption isotherm [32–34,37] is usually used to describe an interfacial segregation phenomenon, which is driven by reduction of interfacial energy. Based on the Gibbs isotherm, theoretical modeling has been recently carried out to quantitatively describe solute segregation at the liquid/substrate interfaces [37]. It has been demonstrated in our research that Ti, Zr or Si in Al melt and Y in Mg melt tend to segregate on the Al/TiB<sub>2</sub> and Mg/MgO interfaces. However, the segregation behavior of the elements is considerably different from one another, leading to the formation of various 2DCs or 2DSs at the interface.

The consequence of the formation of the 2-dimensional segregation layers, the 2DCs or 2DSs, depends on the segregation behavior of different elements at the interfaces, either promoting or impeding heterogeneous nucleation by altering the potency of the substrates. For instance, our research has demonstrated that Ti interfacial segregation makes the synthetic TiB<sub>2</sub> particles as potent as those TiB<sub>2</sub> particles from the commercial Al-Ti-B master alloys in grain refining Al alloys. However, an adverse effect results from by Zr or Si interfacial segregation, due to dissolution of the pre-existing Al<sub>3</sub>Ti 2DC layer and formation of Zr- or Si- enriched 2DC or 2DS. Ultimately, interfacial layers on particle surface determine nucleation potency of substrates. The mechanisms for the consequences are

closely related to the effects resulting from interfacial segregation: (i) change in atomic configuration of substrate surface and, thus, alteration of lattice misfit; (ii) introduction of atomic roughness to substrate surface; and (iii) introduction of chemical reactions between different types of atoms at the interface.

Importantly for Mg alloys, our research demonstrates that native MgO formed in Mg alloy melts is a universal in-situ grain refiner for various Mg alloys. Further search for grain refiner for Mg alloys is not needed [71]. Moreover, interfacial segregation of elements on the MgO surface would allow full use to be made of MgO to achieve significant grain refinement.

From a nucleation point of view, it is possible to manipulate the nucleation process by modification of substrates through deliberate segregation of certain elements. Practically, manipulation of heterogeneous nucleation process can be realized by either promotion or impediment of nucleation potency of substrates through deliberate segregation of desirable elements at the liquid/substrate interfaces, so that both the endogenous and exogenous solid particles can be effectively harnessed to participate in heterogeneous nucleation and the subsequent grain nucleation process. The scientific research has provided us with the basis for development of effective grain refinement methods and alternative grain refiners to alleviate and overcome negative “poisoning” effects.

## 7. Summary and Perspective

Based on assessment of the solidification structures of Al- and Mg- alloys by the TP1 casting process and extensive examinations by the state-of-the-art STEM and associated EDS and EELS of metal/substrate interfaces for  $\text{TiB}_2$ , MgO and  $\text{Al}_2\text{O}_3$  particles in alloy melts, the research work elucidates that alloying elements in Al- and Mg- alloys tend to segregate at the interface, leading to formation of various 2-dimensional compounds (2DCs) or 2-dimensional solution (2DSs), depending upon segregation behavior of the individual elements at different interfaces. The experimental results were verified by STEM-HAADF simulation and ab initio molecular dynamics (AIMD) simulations.

Our current understanding of elemental segregation at interfaces has been advanced and deepened through experimental and theoretical investigations. The exact mechanisms for effective grain refinement, Zr poisoning, and Si poisoning have been a long-standing research topic for the last 70 years in the field of grain refinement. Some of the following arguments in the literature have been settled through clarification by our research: (i) the mechanism of grain refinement by Al-Ti-B grain refiner, (ii) the mechanism of inoculation of  $\text{TiB}_2$  or  $\text{Al}_3\text{Ti}$ , (iii) the mechanisms of Zr poisoning, and (iv) Si poisoning. New concepts, such as 2-dimensional compound (2DC) or solution (2DS), surface roughness at atomic scale, and structural and compositional templating, etc., are proposed in revealing the universal phenomenon of interfacial segregation and its effect on heterogeneous nucleation and grain refinement. In a foundry practice, importantly, manipulation of heterogeneous nucleation process can be realized by either promotion or impediment of nucleation potency of substrates through deliberate segregation of desirable elements on the substrate surfaces, so that both the endogenous and exogenous solid particles can be effectively harnessed to participate in heterogeneous nucleation and the subsequent grain nucleation process. The scientific knowledge provides us with the basis for developments of effective grain refining methods and alternative grain refiners to alleviate and overcome negative “poisoning” effects and achieve desired grain refinement.

**Author Contributions:** Writing-review and editing: Y.W. and Z.F.; Experimental investigation: Y.W., S.W., Z.Q. and C.F.; Technical supports: T.H., X.Z. and Q.M.R.; Supervision: Z.F. All authors have read and agreed to the published version of the manuscript.

**Funding:** This work was financial supported by the EPSRC (UK) for under grant number EP/N007638/1 (Future Liquid Metal Engineering Hub).

**Data Availability Statement:** Not applicable.

**Conflicts of Interest:** The authors declare no conflict of interest.

## References

1. McCartney, D.G. Grain refining of aluminium and its alloys using inoculants. *Int. Mater. Rev.* **1989**, *34*, 247–260. [[CrossRef](#)]
2. Murty, B.S.; Kori, S.A.; Chakraborty, M. Grain refinement of aluminium and its alloys by heterogeneous nucleation and alloying. *Int. Mater. Rev.* **2002**, *47*, 3–47. [[CrossRef](#)]
3. Easton, M.A.; Qian, M.; Prasad, A.; StJohn, D.H. Recent advances in grain refinement of light metals and alloys. *Curr. Opin. Solid State Mater. Sci.* **2016**, *20*, 13–24. [[CrossRef](#)]
4. Queded, T.E. Understanding mechanisms of grain refinement of aluminium alloys by inoculation. *Mater. Sci. Technol.* **2004**, *20*, 1357–1369. [[CrossRef](#)]
5. Greer, L. Overview: Application of heterogeneous nucleation in grain-refining of metals. *J. Chem. Phys.* **2016**, *145*, 211704. [[CrossRef](#)]
6. StJohn, D.H.; Qian, M.; Easton, M.A.; Cao, P.; Hildebrand, Z. Grain refinement of magnesium alloys. *Metall. Mater. Trans. A* **2005**, *36A*, 1669–1679. [[CrossRef](#)]
7. StJohn, D.H.; Easton, M.A.; Qian, M.; Taylor, J.A. Grain refinement of magnesium alloys: A review of recent research, theoretical developments, and their application. *Metall. Mater. Trans. A* **2013**, *44*, 2935–2949. [[CrossRef](#)]
8. Fan, Z. An epitaxial model for heterogeneous nucleation on potent substrates. *Metall. Mater. Trans. A* **2013**, *44*, 1409–1418. [[CrossRef](#)]
9. Jiang, B.; Men, H.; Fan, Z. Atomic ordering in the liquid adjacent to an atomically rough solid surface. *Comp. Mater. Sci.* **2018**, *153*, 73–81. [[CrossRef](#)]
10. Fang, C.M.; Men, H.; Fan, Z. Effect of substrate chemistry on prenucleation. *Metall. Mater. Trans. A* **2018**, *49*, 6231–6242. [[CrossRef](#)]
11. Fan, Z.; Wang, Y.; Zhang, Y.; Qin, T.; Zhou, X.; Thompson, G.E.; Pennycook, T.; Hashimoto, T. Grain refining mechanism in the Al/Al-Ti-B system. *Acta Mater.* **2015**, *84*, 292–304. [[CrossRef](#)]
12. Jones, G.P.; Pearson, J. Factors affecting the grain-refinement of aluminium using titanium and boron additives. *Metall. Trans. B* **1976**, *7*, 223–234. [[CrossRef](#)]
13. Birch, M.E.J.; Fisher, P. Grain refining of commercial aluminium alloys with titanium boron aluminium. In *Aluminium Technology '86: Proceedings of the International Conference*; Shepard, T., Ed.; The Institute of Metals: London, UK, 1986; pp. 117–124.
14. Ahmady, S.M.; McCartney, D.G.; Thistlethwaite, S.R. Assessment of aluminium grain refiner performance using the ALCOA test. In *Light Metals 1990*; Bickert, C.M., Ed.; TMS: Warrendale, PA, USA, 1990; pp. 837–843.
15. Kearns, M.A.; Cooper, P. Effects of solutes on grain refinement of selected wrought aluminium alloys. *Mater. Sci. Technol.* **1997**, *13*, 650–654. [[CrossRef](#)]
16. Birch, M.E.J.; Cowell, A.J.J. Grain refinement of aluminium alloys containing chromium and zirconium. In *Solidification Processing 1987*; Beech, J., Jones, H., Eds.; The Institute of Metals: London, UK, 1988; pp. 149–152.
17. Abdel-Hamid, A.A. Effect of other elements on the grain refinement of Al by Ti or Ti and B. Part I—A critical review. *Z. Metallkd.* **1989**, *80*, 566–569.
18. Abdel-Hamid, A.A. Effect of other elements on the grain refinement of aluminum by titanium or titanium and boron. Part II. Effect of the refractory metals vanadium, molybdenum, zirconium, and tantalum. *Z. Metallkd.* **1989**, *80*, 643–647.
19. Sigworth, G.K.; Guzowaski, M.M. Grain refining of hypoeutectic Al-Si alloys. *AFS Trans.* **1985**, *93*, 907–912.
20. Johnsson, M. Influence of Si and Fe on the grain refinement of aluminium. *Z. Metallk.* **1994**, *85*, 781–785. [[CrossRef](#)]
21. Spittle, J.A.; Keeble, J.M.; Al Meshhedani, M. The grain refinement of Al-Si foundry alloys. In *Light Metals 1997*; Huglen, R., Ed.; TMS: Warrendale, PA, USA, 1997; pp. 795–800.
22. Hutt, J.E.C.; StJohn, D.H.; Hogan, L.; Dahle, A.K. Equiaxed solidification of Al-Si alloys. *Mater. Sci. Technol.* **1999**, *15*, 495–500. [[CrossRef](#)]
23. Lee, Y.C.; Dahle, A.K.; StJohn, D.H.; Hutt, J.E.C. The effect of grain refinement and silicon content on grain formation in hypoeutectic Al-Si alloys. *Mater. Sci. Eng. A* **1999**, *259*, 43–52. [[CrossRef](#)]
24. Birol, Y. Effect of silicon content in grain refining hypoeutectic Al-Si foundry alloys with boron and titanium additions. *Mater. Sci. Technol.* **2012**, *28*, 385–389. [[CrossRef](#)]
25. Kori, S.A.; Auradi, V.; Murty, B.S.; Chakraborty, M. Poisoning and fading mechanism of grain refinement in Al-7Si alloy. *Mater. Forum* **2005**, *29*, 387–393.
26. Wang, Y.; Fang, C.M.; Zhou, L.; Hashimoto, T.; Zhou, X.; Ramasse, Q.M.; Fan, Z. Mechanism for Zr poisoning of Al-Ti-B based grain refiners. *Acta Mater.* **2019**, *164*, 428–439. [[CrossRef](#)]
27. Wang, Y.; Zhou, L.; Fan, Z. Mechanism of zirconium poisoning effect on TiB<sub>2</sub> inoculation in aluminium alloys. In *Light Metals 2016*; Williams, E., Ed.; TMS: Warrendale, PA, USA, 2016; pp. 725–729.
28. Wang, S.H.; Wang, Y.; Ramasse, Q.M.; Schmid-Fetzer, R.; Fan, Z. Segregation of yttrium at Mg/MgO interface in Mg-Y alloy. *Acta Mater.* **2022**.
29. Wang, S.H. Characterisation of Native MgO and Its Roles in Solidification of Mg Alloys. Ph.D. Thesis, Brunel University London, London, UK, 2020.

30. Wang, Y.; Que, Z.P.; Hashimoto, T.; Zhou, X.; Fan, Z. Mechanism for Si poisoning of Al-Ti-B grain refiners in Al alloys. *Metall. Mater. Trans. A* **2020**, *51*, 5743–5757. [[CrossRef](#)]
31. Hofmann, S. Thermodynamics of interfacial segregation in metals and ceramics. *J. Chem. Phys.* **1987**, *84*, 141–147. [[CrossRef](#)]
32. Gibbs, J.W. *The Collected Works of J. Willard Gibbs*; Yale University Press: New Haven, CT, USA, 1948.
33. Hondros, E.; Seah, M.; Hofmann, S.; Lejcek, P. *Physical Metallurgy*, 4th ed.; Cahn, R., Haasen, P., Eds.; Elsevier: Amsterdam, The Netherlands, 1996; pp. 1202–1289.
34. McBain, J.W.; Mills, G.F. The adsorption theorem of J. Willard Gibbs. Anomalies in applying it to surface tension curves that exhibit minima in dilute solution. *Rep. Prog. Phys.* **1938**, *5*, 30–45. [[CrossRef](#)]
35. Christian, J.W. *The Theory of Transformations in Metals and Alloys*, 3rd ed.; Pergamon: Oxford, UK, 2002.
36. Cantor, B. Heterogeneous nucleation and adsorption. *Philos. Trans. R. Soc. Lond. A* **2003**, *361*, 409–417. [[CrossRef](#)]
37. Men, H.; Fan, Z. An analytical model for solute segregation at liquid metal/solid substrate interface. *Metall. Mater. Trans. A* **2014**, *45*, 5508–5516. [[CrossRef](#)]
38. Schumacher, P.; Greer, A.L. Heterogeneously nucleated  $\alpha$ -Al in amorphous aluminium alloys. *Mater. Sci. Eng. A* **1994**, *178*, 309–313. [[CrossRef](#)]
39. Schumacher, P.; Greer, A.L. Enhanced heterogeneous nucleation of  $\alpha$ -Al in amorphous aluminium alloys. *Mater. Sci. Eng. A* **1994**, *181–182*, 1335–1339. [[CrossRef](#)]
40. Fan, Z.; Wang, Y.; Xia, M.; Arumuganathar, S. Enhanced heterogeneous nucleation in AZ91D alloy by intensive melt shearing. *Acta Mater.* **2009**, *57*, 4891–4901. [[CrossRef](#)]
41. Wang, Y.; Fan, Z.; Zhou, X.; Thompson, G.E. Characterisation of magnesium oxide and its interface with  $\alpha$ -Mg in Mg-Al based alloys. *Phil. Mag. Lett.* **2011**, *91*, 516–529. [[CrossRef](#)]
42. Koch, C. Determination of Core Structure Periodicity and Point Defect Density Along Dislocations. Ph.D. Thesis, Arizona State University, Tempe, AR, USA, January 2002.
43. Verwey, E.J.W. The crystal structure of  $\gamma$ -Fe<sub>2</sub>O<sub>3</sub> and  $\gamma$ -Al<sub>2</sub>O<sub>3</sub>. *Z. Kristallogr.* **1935**, *91*, 65–69. [[CrossRef](#)]
44. Fang, C.M.; Yasmin, S.; Fan, Z. Interfacial interaction and prenucleation at liquid-Al/ $\gamma$ -Al<sub>2</sub>O<sub>3</sub>{1 1 1} interfaces from ab initio molecular dynamics simulations. *J. Phys. Comm.* **2021**, *5*, 015007. [[CrossRef](#)]
45. Fiquet, G.; Richet, P.; Montagnac, G. High-temperature thermal expansion of lime, periclase, corundum and spinel. *Phys. Chem. Min.* **1999**, *27*, 103–111. [[CrossRef](#)]
46. Kresse, G.; Furthmüller, J. Efficiency of ab initio total energy calculations for metals and semiconductors using a plane-wave basis set. *Comp. Mater. Sci.* **1996**, *6*, 15–50. [[CrossRef](#)]
47. Blöchl, P.E. Projector augmented-wave method. *Phys. Rev. B* **1994**, *50*, 17953–17978. [[CrossRef](#)]
48. Perdew, J.P.; Burke, K.; Ernzerhof, M. Generalized gradient approximation made simple. *Phys. Rev. Lett.* **1996**, *77*, 3865–3868. [[CrossRef](#)]
49. Monkhorst, H.J.; Pack, J.D. Special points for Brillouin-zone integrations. *Phys. Rev. B* **1976**, *13*, 5188–5192. [[CrossRef](#)]
50. Fang, C.M.; Fan, Z. Atomic ordering at the liquid-Al/MgAl<sub>2</sub>O<sub>4</sub>{1 1 1} interfaces: Ab initio molecular dynamics simulations. *Metall. Mater. Trans. A* **2020**, *51*, 6318–6326. [[CrossRef](#)]
51. Hintzsche, L.E.; Fang, C.M.; Watts, T.; Marsman, M.; Jordan, G.; Lamers, M.W.P.E.; Weeber, A.W.; Kresse, G. Density functional theory study of the structural and electronic properties of amorphous silicon nitrides: Si<sub>3</sub>N<sub>4</sub>-x:H. *Phys. Rev. B* **2012**, *86*, 235204. [[CrossRef](#)]
52. Marx, D.; Hutter, J. *Ab Initio Molecular Dynamics: Basic Theory and Advanced Methods*; Cambridge University Press: Cambridge, UK, 2009.
53. *AA TP1*; Standard Test Procedure for Aluminium Alloy Grain Refiners (TP-1). The Aluminium Association: Washington, DC, USA, 1990.
54. Wang, Y.; Petal, J.B.; Zhang, Y.; Fan, Z. *Examination of Commercial Al-5Ti-1B Grain Refiners from MQP Ltd and STNM Ltd*, Technical Report; MQP Ltd: Solihull, UK, 2021.
55. Fan, Z.; Men, H.; Wang, Y.; Que, Z.P. A new atomistic mechanism for heterogeneous nucleation in the systems with negative lattice misfit: Creating a 2D template for crystal growth. *Metals* **2021**, *11*, 478. [[CrossRef](#)]
56. Greer, A.L.; Bunn, A.M.; Tronche, A.; Evans, P.V.; Bristow, D.J. Modelling of inoculation of metallic melts: Application to grain refinement of aluminium by Al-Ti-B. *Acta Mater.* **2000**, *48*, 2823–2835. [[CrossRef](#)]
57. Qin, T.; Fan, Z. Molecular analysis of grain refining in aluminium with Al-5Ti-B. *IOP Conf. Ser. Mater. Sci. Eng.* **2011**, *27*, 012007.
58. Wang, J.; Horsfield, A.; Schwingenschlögl, U.; Lee, P.D. Heterogeneous nucleation of solid Al from the melt by TiB<sub>2</sub> and Al<sub>3</sub>Ti: An ab initio molecular dynamics study. *Phys. Rev. B* **2010**, *82*, 184203. [[CrossRef](#)]
59. Ma, S.; Yan, R.; Jing, T.; Dong, H. Substrate-induced liquid layering: A new insight into the heterogeneous nucleation of liquid metals. *Metals* **2018**, *8*, 521. [[CrossRef](#)]
60. Dolukhanyan, S.K.; Aleksanyan, A.G.; Ter-Galstyan, O.P.; Shekhtman, V.S.; Sakharov, M.K.; Abrosimova, G.E. Specifics of the formation of alloys and their hydrides in Ti-Zr-H system. *Russ. J. Phys. Chem. B* **2007**, *1*, 563–569. [[CrossRef](#)]
61. Khaliq, A.; Rhamdhani, M.A.; Brooks, G.A.; Grandfield, J. Thermodynamic analysis of Ti, Zr, V and Cr impurities in aluminium melt. In *Light Metals 2011*; Lindsay, S.J., Ed.; TMS: Warrendale, PA, USA, 2011; pp. 751–756.
62. Farrar, P.A.; Adler, S. On the system titanium-zirconium. *Trans. Metall. Soc. AIME* **1996**, *236*, 1061–1064.
63. Men, H.; Fan, Z. Prenucleation induced by crystalline substrates. *Metall. Mater. Trans. A* **2018**, *49*, 2766–2777. [[CrossRef](#)]

64. Que, Z.P.; Zhou, Y.P.; Xia, J.H.; Wang, Y.; Fang, C.M.; Mendis, C.L.; Fan, Z. Heterogeneous nucleation and refinement of Fe-containing intermetallic compounds in Al alloys. In *The Future Liquid Metal Engineering Hub, Report 2015–2021*; LiME: Uxbridge, UK, 2021; pp. 44–45. Available online: <https://www.lime.ac.uk/blog/2021-annual-report-published> (accessed on 1 October 2021).
65. Que, Z.P.; Wang, Y.; Mendis, C.L.; Fang, C.M.; Xia, J.H.; Zhou, X.R.; Fan, Z. Formation, morphology control and refinement of Fe-containing intermetallic compounds in Al alloys: An overview. *Metals*, 2022; *in press*.
66. Que, Z.P.; Zhou, Y.P.; Wang, Y.; Fan, Z. Composition templating for heterogeneous nucleation of intermetallic compounds. In *SP'17-Solidification Processing 2017*; Fan, Z., Ed.; Brunel University London: Uxbridge, UK, 2017; pp. 158–161.
67. Que, Z.; Wang, Y.; Fan, Z. Heterogeneous nucleation of eutectic structure in Al-Mg-Si alloys. *Metall. Mater. Trans. A* **2020**, *51*, 2697–2702. [[CrossRef](#)]
68. Fan, Z.; Que, Z.; Wang, Y.; Jiang, B. Structural and compositional templating for heterogeneous nucleation. In *Frontiers in Solidification*; Kurz, W., Dantzig, J., Karma, A., Hoyt, J., Eds.; Symposium in honour of Michel Rappaz; TMS: Warrendale, PA, USA, 2016; pp. 17–21.
69. Li, J.; Hage, F.S.; Ramasse, Q.M.; Schumacher, P. The nucleation sequence of  $\alpha$ -Al on TiB<sub>2</sub> particles in Al-Cu alloys. *Acta Mater.* **2021**, *206*, 116652. [[CrossRef](#)]
70. Wang, S.H.; Wang, Y.; Ramasse, Q.; Fan, Z. The nature of native MgO in Mg and its alloys. *Metall. Mater. Trans. A* **2020**, *51*, 2957–2974. [[CrossRef](#)]
71. Wang, Y.; Peng, G.S.; Fan, Z. Grain refinement of Mg and its alloys by inoculation of in situ MgO particles. In *Magnesium Technology 2017*; Solanki, K.N., Orlov, D., Singh, A., Neelameggham, N.R., Eds.; TMS: Warrendale, PA, USA, 2017; pp. 99–106.
72. Fan, Z.; Wang, Y.; Zhang, Z.F.; Xia, M.; Li, H.T.; Xu, J.; Granasy, L.; Scamans, G.M. Shear enhanced heterogeneous nucleation in some Mg- and Al- alloys. *Int. J. Cast Metals Res.* **2009**, *22*, 318–322. [[CrossRef](#)]
73. Wang, Y.; Xia, M.; Fan, Z.; Zhou, X.; Thompson, G.E. The effect of Al<sub>8</sub>Mn<sub>5</sub> intermetallic particles on grain size of as-cast Mg-Al-Zn AZ91D alloy. *Intermetallics* **2010**, *18*, 1683–1689. [[CrossRef](#)]
74. Fan, Z.; Gao, F.; Wang, Y.; Wang, S.H.; Petal, J.B. Grain refining of Mg-alloys by native MgO particles: An overview. *J. Magnes. Alloy.* **2022**, *in press*.
75. Wang, Y.; Li, H.T.; Fan, Z. Grain refinement of Al- and Mg- alloys by native oxide particles. In *Solidification Processing 2017*; Fan, Z., Ed.; Brunel University London: Uxbridge, UK, 2017; pp. 81–86.
76. Peng, G.S.; Wang, Y.; Fan, Z. Competitive heterogeneous nucleation between Zr and MgO particles in commercial purity magnesium. *Metall. Mater. Trans. A* **2018**, *49*, 2182–2192. [[CrossRef](#)]
77. Wang, S.H.; Wang, F.; Wang, Y.; Ramasse, Q.M.; Fan, Z. Segregation of Ca at the Mg/MgO interface and its effect on grain refinement of Mg alloys. *Mater. Sci. Eng.* **2019**, *529*, 012048. [[CrossRef](#)]
78. Zuo, Y.B.; Xia, M.X.; Liang, S.M.; Wang, Y.; Scamans, G.M.; Fan, Z. Grain refinement of DC cast AZ91D Mg alloy by intensive melt shearing. *Mater. Sci. Technol.* **2011**, *27*, 101–107. [[CrossRef](#)]
79. Liu, G.; Wang, Y.; Fan, Z. A physical approach to the direct recycling of Mg-alloy scrap by the rheo-diecasting process. *Mater. Sci. Eng. A* **2008**, *472*, 251–257. [[CrossRef](#)]
80. Fan, Z.; Gao, F.; Jiang, B.; Que, Z. Impeding nucleation for more significant grain refinement. *Sci. Rep.* **2020**, *10*, 9448. [[CrossRef](#)]
81. Men, H.; Jiang, B.; Fan, Z. Mechanisms of grain refinement by intensive shearing of AZ91 alloy melt. *Acta Mater.* **2010**, *58*, 6526–6534. [[CrossRef](#)]
82. Fang, C.M.; Fan, Z. Prenucleation at the interface between MgO and liquid magnesium: An ab initio molecular dynamics study. *Metall. Mater. Trans. A* **2020**, *51*, 788–797.
83. Katagiri, S.; Ishizawa, N.; Marumo, F. A new high temperature modification of face-centered cubic Y<sub>2</sub>O<sub>3</sub>. *Powder Diffr.* **1993**, *8*, 60. [[CrossRef](#)]
84. Takeuchi, A.; Inoue, A. Classification of bulk metallic glasses by atomic size difference, heat of mixing and period of constituent elements and its application to characterization of the main alloying element. *Mater. Trans.* **2005**, *41*, 846–829.
85. Narayanan, L.A.; Samuel, F.H.; Gruzleski, J.E. Crystallization behaviour of iron-containing intermetallic compounds in 319 aluminium alloy. *Metall. Mater. Trans. A* **1994**, *25*, 1761–1773. [[CrossRef](#)]
86. Wang, Y.; Li, H.T.; Fan, Z. Oxidation of aluminium alloy melts and inoculation by oxide particles. *Trans. Indian Inst. Met.* **2012**, *65*, 653–661. [[CrossRef](#)]
87. Li, H.T.; Wang, Y.; Xia, M.; Zuo, Y.; Fan, Z. Harnessing oxides in liquid metals and alloys. In *Solidification Science and Technology: Proceedings of the John Hunt International Symposium 12–14 December 2011, Brunel University, UK*; Fan, Z., Stone, I.C., Eds.; Brunel University Press: Uxbridge, UK, 2011; pp. 93–110.
88. Wang, S.H.; Fang, C.M.; Wang, Y.; Lordan, E.; Fan, Z. Segregation of La at Al/ $\gamma$ -Al<sub>2</sub>O<sub>3</sub> interface. *Acta Mater.* **2022**, *submitted*.
89. Li, H.T.; Wang, Y.; Fan, Z. Mechanisms of heterogeneous nucleation during solidification in binary Al-Mg alloys. *Acta Mater.* **2012**, *60*, 1528–1537.
90. Cibula, A. The effect of C and B in the grain refinement of sand casting in aluminium alloys. *J. Inst. Met.* **1951**, *80*, 1–16.
91. Johnsson, M.; Bäckerud, L.; Sigworth, G.K. Study of the mechanism of grain refinement of aluminium after additions of Ti and B-containing master alloys. *Metall. Trans. A* **1993**, *24*, 481–491.
92. Quedstedt, T.E.; Greer, A.L. The effect of the size distribution of inoculant particles on as-cast crystal size in aluminium alloys. *Acta Mater.* **2004**, *52*, 3859–3868.